ALMA survey of circumstellar discs in the young stellar cluster IC 348

D. Ruíz-Rodríguez,[1,2]★ L. A. Cieza,[3,4] J. P. Williams,[5] S. M. Andrews,[6] D. A. Principe,[7] C. Caceres,[8,12] H. Canovas,[9] S. Casassus,[3,10] M. R. Schreiber[3,11,12] and J. H. Kastner[1]

[1]*Chester F. Carlson centre for Imaging Science, School of Physics & Astronomy, and Laboratory for Multiwavelength Astrophysics, Rochester Institute of Technology, 54 Lomb Memorial Drive, Rochester, NY 14623 USA*
[2]*Research School of Astronomy and Astrophysics, Australian National University, Canberra ACT 2611, Australia*
[3]*Millenium Nucleus 'Protoplanetary discs in ALMA Early Science', 8370191 Chile*
[4]*Núcleo de Astronomía, Facultad de Ingeniería, Universidad Diego Portales, Av. Ejercito 441, Santiago NAN, Chile*
[5]*Institute for Astronomy, University of Hawaii at Manoa, Honolulu, HI 96822, USA*
[6]*Harvard-Smithsonian centre for Astrophysics, 60 Garden Street, Cambridge, MA 02138, USA*
[7]*Department of Physics and Kavli Institute for Astrophysics and Space Research, Massachusetts Institute of Technology, Cambridge, MA 02139, USA*
[8]*Departamento de Ciencias Fisicas, Facultad de Ciencias Exactas, Universidad Andres Bello. Av. Fernandez Concha 700, Las Condes, Santiago NAN, Chile*
[9]*European Space Astronomy Centre (ESA), Camino Bajo del Castillo s/n, 28692 Villanueva de la Cañada, Madrid, Spain*
[10]*Universidad de Chile, Camino el Observatorio 1515, Santiago 7591245, Chile*
[11]*Instituto de Fsica y Astronoma, Universidad de Valparaso, Av. Gran Bretaa 1111, 2360102 Valparaso, Chile*
[12]*Núcleo Milenio Formación Planetaria - NPF, Universidad de Valparaiso, Av. Gran Bretaña 1111, Valparaiso, Chile*

ABSTRACT

We present a 1.3 mm continuum survey of the young (2–3 Myr) stellar cluster IC 348 that lies at a distance of 310 pc and is dominated by low-mass stars ($M_\star \sim$ 0.1–0.6 $M_\odot$). We observed 136 Class II sources (discs that are optically thick in the infrared) at 0.8 arcsec (200 au) resolution with a 3σ sensitivity of $\sim$0.45 mJy ($M_{dust} \sim 1.3\,M_\oplus$). We detect 40 of the targets and construct a mm-continuum luminosity function. We compare the disc mass distribution in IC 348 to those of younger and older regions, taking into account the dependence on stellar mass. We find a clear evolution in disc masses from 1 to 5–10 Myr. The disc masses in IC 348 are significantly lower than those in Taurus (1–3 Myr) and Lupus (1–3 Myr), similar to those of Chamaleon I, (2–3 Myr) and σ Ori (3–5 Myr) and significantly higher than in Upper Scorpiusrpius (5−10 Myr). About 20 discs in our sample ($\sim$5 per cent of the cluster members) have estimated masses (dust + gas) > $1 M_{Jup}$ and hence might be the precursors of giant planets in the cluster. Some of the most massive discs include transition objects with inner opacity holes based on their infrared Spectral Energy Distribution (SEDs). From a stacking analysis of the 96 non-detections, we find that these discs have a typical dust mass of just $\lesssim$0.4 $M_\oplus$, even though the vast majority of their infrared SEDs remain optically thick and show little signs of evolution. Such low-mass discs may be the precursors of the small rocky planets found by *Kepler* around M-type stars.

Key words: instrumentation: interferometers – planetary systems.

1 INTRODUCTION

The evolution of protoplanetary discs has been studied for decades, and typical disc lifetimes are well established to be $\sim$2–3 Myr (Williams & Cieza 2011). On this time-scale, the dust and gas components undergo significant evolution that, together with the initial conditions, determines the outcome of the planet-formation process. By an age of $\sim$5 Myr, around 90 per cent of protoplanetary discs have already dispersed, constraining the time available for

most planets to be formed (Sicilia-Aguilar et al. 2006). Determining the main process of disc dispersal is not an easy task since several physical mechanisms play a role at different time-scales and radii (Alexander et al. 2014), but studying disc properties as a function of stellar mass and age can shed light on the frequency and location of forming planets (Mordasini et al. 2012; Alibert, Mordasini & Benz 2011).

One important inference from exoplanet surveys is that planet occurrence generally decreases with increasing planet size: rocky planets are much more common than gas giants (Howard et al. 2012; Bonfils et al. 2013; Burke et al. 2015). Moreover, the correlation between stellar and planet properties indicates that giant planet

★ E-mail: daryalexia@gmail.com (DR) lucas.cieza@mail.udp.cl (LAC)

occurrence increases with stellar mass at solar metallicity, with a percentage of 3 per cent around M dwarfs ($\sim$0.5 M$_\odot$) increasing to 14 per cent around A stars ($\sim$2 M$_\odot$, Johnson et al. 2010). These exoplanet correlations are likely to be connected to disc properties as functions of stellar mass.

$^{1.5-2.0}$Emission from mm-sized dust grains in the disc is generally optically thin in the (sub-)mm regime; therefore, (sub-)mm continuum surveys of discs in star-forming regions with different ages ($\sim$1$-$10Myr) can trace the distribution of disc masses as a function of age and stellar mass. This allows us to investigate how disc properties and evolution connect to the population of planets observed in the field. To exploit this observational potential, Andrews et al. (2013) performed a mm continuum survey with the Submm Array of the Taurus Class II members (optically thick discs) with spectral types earlier than M8.5. As a main result, they showed a correlation between the mm luminosity (L_{mm}) and the mass of the host stellar object of the form $L_{mm} \propto M_*$ that in turn suggests a linear relationship between the masses of the disc and that of the parent star: $M_{dust} \propto M_*$.

Various observational studies of higher sensitivity and resolution with the Atacama Large mm/submm Array (ALMA) add additional samples in Lupus (1–3 Myr; Comeron 2008; Alcalá et al. 2014; Ansdell et al. 2016), Chamaeleon I (2–3 Myr; Luhman 2007; Pascucci et al. 2016), σ Ori (3–5 Myr; Oliveira et al. 2002; Ansdell et al. 2016), and the Upper Scorpius OB Association (5–10 Myr; Pecaut, Mamajek & Bubar 2012; Barenfeld et al. 2016). A Bayesian linear regression has been the standard method used to characterize the $M_{dust}-M_*$ relations of these star-forming regions. Although, initially M_{dust} and M_* were thought to be linearly correlated in 1$-$3 Myr old clusters, the main caveat of these linear relations is the simultaneous fitting of detections and upper limits that is complicated by the fact that the latter dominates the aforementioned surveys. This adds more uncertainty to the $M_{dust}-M_*$ relationship because the limited sensitivity implies lower detection rates for late-type stars and brown dwarfs, allowing for the possibility of a steeper relation. Indeed, Pascucci et al. (2016) reanalysed all the (sub-)mm fluxes and stellar properties available for Taurus, Lupus, and Upper Scorpius, and found steeper correlations than linear for these clusters. They also obtained a steep dust mass–stellar mass scaling relation in the $\sim$2 Myr Cha I star-forming region, hence concluding that the same $M_{dust}-M_*$ relation is shared by star-forming regions that are 1–3 Myr old (Pascucci et al. 2016). More recently, a similar steepening of the $M_{dust}-M_*$ relation was found by Ansdell et al. (2017) for the σ Ori star-forming region. This steeper relation possibly indicates (1) undetected large pebbles or (2) an efficient inward drift in discs around the lowest mass stars. In addition, this steepening of the $M_{dust}-M_*$ correlation with age suggests a faster decline of circumstellar dust mass with time in late-type stars. From these relations, at an age of $\lesssim$10 Myr, discs around 0.1 and 0.5 M$_\odot$ stars might have dispersed mm-sized grains by factors of 5 and 2.5, respectively, faster than earlier-type objects (Pascucci et al. 2016).

Following these studies, the IC 348 star-forming region, with a disc fraction of 36 per cent in the Infrared (IR) regime, is an excellent benchmark to characterize the relationship between the masses of the disc and that of the host star by comparing to other star-forming regions. In fact, the first mm observations of protoplanetary discs in IC 348 star-forming region were made by Lee, Williams & Cieza (2011), and with a detection rate of only $\sim$12 per cent, they concluded that most of the solids in the IR-detected discs have aggregated beyond mm sizes, resulting in low luminosities at mm wavelengths.
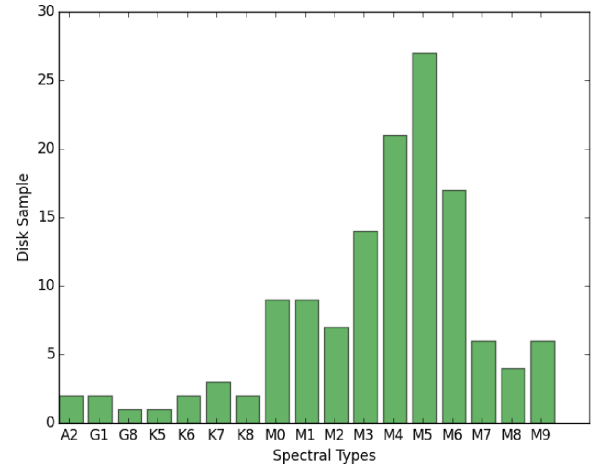

Figure 1. Distribution of stellar spectral types for our sample in the IC 348 star-forming region. These targets were selected from Muench et al. (2007) and Lada et al. (2006) and are listed in Table 1.

In this work, we present a 1.3 mm/230 GHz study of $\sim$136 Class II objects in the IC 348 star-forming region. This paper is organized as follows: Section 2 describes the target selection. Section 3 summarizes the ALMA observations and data reduction. In Section 4, we estimate the stellar properties of our sample, and present our ALMA results that are compared to previous findings in other regions in Section 5. The main conclusions are discussed in Section 6.

2 TARGET SELECTION AND PROPERTIES

IC 348 is a rich and compact (2 pc $\times$ 2 pc) young stellar cluster in the Perseus molecular cloud, whose $\sim$480 members have been identified initially by H α emission (Herbig 1954) and subsequently by optical and IR photometry and spectroscopy (Lada & Lada 1995; Herbig 1998; Luhman et al. 1998; Luhman 1999; Luhman et al. 2003; Luhman 2003, 1999; Luhman, McLeod & Goldenson 2005; Luhman, Esplin & Loutrel 2016). Most of the known T Tauri stars in the IC 348 star-forming region have been well studied and spectrally classified (Luhman et al. 2003; Muench et al. 2007): see Fig. 1.

Our sample was selected specifically from the work of Lada et al. (2006), whose sample was based on Luhman et al. (2003), and from Muench et al. (2007), a census of 192 candidate Young Stellar Objects (YSOs) in the IC 348 nebula, covering a 26.8 arcmin $\times$ 28.5 arcmin region and centred at RA 0344^{mh}20^{s}52, Dec. +32°10$'$34$''$87. These programs used *Spitzer*–IRAC photometry to investigate both the frequency and nature of the circumstellar disc population in the IC 348 cluster on the basis of the IR SED slope between 3.6 and 8.0 μm, $\alpha_{3.6-8.0\,\mu m}$. In general, Lada et al. (2006) and Muench et al. (2007) used $\alpha_{3.6-8.0\,\mu m}$ to classify the objects as follows:

(i) Class I (protostars): $\alpha_{3.6-8.0\,\mu m} > -0.5$;
(ii) Class II (thick-discs): $-0.5 > \alpha_{3.6-8.0\,\mu m} > -1.8$;
(iii) Class II/III (anemic discs): $-1.8 > \alpha_{3.6-8.0\,\mu m} > -2.56$;
(iv) Class III (disc-less stars): $\alpha_{3.6-8.0\,\mu m} < -2.56$.

Lada et al. (2006) classified as 'anemic discs' those objects with $-1.8 > \alpha_{3.6-8.0\,\mu m} > -2.56$, while Muench et al. (2007) did not search for members with 'anemic' type discs. Hence, we selected *Spitzer* sources with $\alpha_{3.6-8.0\,\mu m}$ values between -1.8 and -0.5 that correspond to Class II T Tauri stars with optically thick discs. From Lada et al. (2006), we selected 91 objects classified as optically

Table 1. Targeted Class II Objects in IC 348.

Source ID	Target	RA	Dec.	Spec. type	Ref.
1	IC 348 12	03 44 35.34	+32 10 04.88	A2	1
2	V∗ V909 Per	03 44 26.03	+32 04 30.41	G8	1
3	Cl∗ IC 348 LRL 13	03 43 59.65	+32 01 53.98	M0.5	1
4	V∗ V926 Per	03 44 44.72	+32 04 02.48	M0.5	1
5	Cl∗ IC 348 LRL 19	03 44 30.82	+32 09 55.80	A2	1
6	Cl∗ IC 348 LRL 26	03 43 56.03	+32 02 13.21	K7	1
7	V∗ V920 Per	03 44 37.88	+32 08 04.18	K7	1
8	V∗ V715 Per	03 44 38.46	+32 07 35.70	K6	1
9	V∗ V712 Per	03 44 37.98	+32 03 29.66	K6	1
10	V∗ V910 Per	03 44 29.73	+32 10 39.84	K8	1
11	V∗ V697 Per	03 44 21.61	+32 10 37.68	K7	1
12	Cl∗ IC 348 LRL 46	03 44 11.62	+32 03 13.18	−	1
13	IRAS 03410+3152	03 44 12.98	+32 01 35.50	−	1
14	Cl∗ IC 348 LRL 55	03 44 31.37	+32 00 14.05	M0.5	1
15∗	V∗ V716 Per	03 44 38.54	+32 08 00.65	M1.25	1, 3
16	V∗ V698 Per	03 44 22.29	+32 05 42.79	K8	1
17	Cl∗ IC 348 LRL 63	03 43 58.91	+32 11 27.07	M1.75	1
18	Cl∗ IC 348 LRL 68	03 44 28.51	+31 59 54.00	M3.5	1
19	V∗ V719 Per	03 44 43.77	+32 10 30.41	M1.25	1
20	Cl∗ IC 348 LRL 76	03 44 39.80	+32 18 04.19	M3.75	1
21	V∗ V710 Per	03 44 37.41	+32 09 00.91	M1	1
22	V∗ V922 Per	03 44 39.20	+32 09 44.90	M2	1
23∗	Cl∗ IC 348 LRL 97	03 44 25.55	+32 06 17.13	M2.25	1,3
24	V∗ V695 Per	03 44 19.24	+32 07 34.74	M3.75	1
25	V∗ V905 Per	03 44 22.32	+32 12 00.70	M1	1
26	V∗ V925 Per	03 44 44.59	+32 08 12.54	M2	1
27	V∗ V919 Per	03 44 37.39	+32 12 24.20	M2	1
28	Cl∗ IC 348 LRL 128	03 44 20.18	+32 08 56.59	M2	1
29	Cl∗ IC 348 LRL 129	03 44 21.30	+32 11 56.34	M2	1
30∗	Cl∗ IC 348 LRL 135	03 44 39.18	+32 20 08.93	M4.5	1,3
31	V∗ V907 Per	03 44 25.30	+32 10 12.80	M4.75	1
32	Cl∗ IC 348 LRL 140	03 44 35.69	+32 03 03.54	M3.25	1
33	Cl∗ IC 348 LRL 149	03 44 36.98	+32 08 34.20	M4.75	1
34	Cl∗ IC 348 LRL 153	03 44 42.76	+32 08 33.77	M4.75	1
35	Cl∗ IC 348 LRL 156	03 44 06.78	+32 07 54.09	M4.25	1
36	V∗ V902 Per	03 44 18.58	+32 12 53.08	M2.75	1
37	Cl∗ IC 348 LRL 165	03 44 35.46	+32 08 56.35	M5.25	1
38	Cl∗ IC 348 LRL 166A	03 44 42.58	+32 10 02.50	M4.25	1
39	Cl∗ IC 348 LRL 168	03 44 31.35	+32 10 46.98	M4.25	1
40	Cl∗ IC 348 LRL 173	03 44 10.13	+32 04 04.50	M5.75	1
41	Cl∗ IC 348 LRL 192	03 44 23.65	+32 01 52.69	M4.5	1
42	V∗ V713 Per	03 44 38.01	+32 11 37.03	M4	1
43	Cl∗ IC 348 LRL 202	03 44 34.28	+32 12 40.73	M3.5	1
44	Cl∗ IC 348 LRL 203	03 44 18.10	+32 10 53.44	M0.75	1
45	Cl∗ IC 348 LRL 205	03 44 29.80	+32 00 54.58	M6	1
46	Cl∗ IC 348 LRL 214	03 44 07.51	+32 04 08.81	M4.75	1
47	Cl∗ IC 348 LRL 221	03 44 40.24	+32 09 33.13	M4.5	1
48	SSTc2d J034431.2+320559	03 44 31.19	+32 05 58.90	M0.5	1
49∗	Cl∗ IC 348 LRL 229	03 44 57.86	+32 04 01.60	M5.25	1, 3
50	Cl∗ IC 348 LRL 237	03 44 23.57	+32 09 33.88	M5	1

'THICK' discs (hereafter Class II sources to keep the nomenclature consistent) and from Muench et al. (2007), we selected 42 objects classified as Class II objects. We also included Cl∗ IC 348 LRL 31, Cl∗ IC 348 LRL 67, and Cl∗ IC 348 LRL 329 that are Class III sources based on their $\alpha_{3.6-8.0\,\mu m}$ values, but their 24 μm fluxes indicate that they are transitional objects with optically thick outer discs (Lada et al. 2006; Espaillat et al. 2012).

We note that the standard YSO class system (Greene et al. 1994) is based on the SED slope between ∼2 and ∼20 μm, but most IC 348 members lack *Spitzer* 24 μm detections. With these caveats, our final target list (Table 1) is composed of 136 Class II disc objects with stellar spectral types in the range of G1−M9. Fig. 2 shows the positions of our targets. Among the objects selected, Cl∗ IC 348 LRL 237, V∗ V716 Per, Cl∗ IC 348 LRL 135, and Cl∗ IC 348 LRL 97 are classified by Espaillat et al. (2012) as transitional discs. Our sample also includes Cl∗ IC 348 LRL 31 and Cl∗ IC 348 LRL 135 that have known close stellar companions at separations of 38.1± 5.3 and 82.1± 0.3 mas, respectively (Ruíz-Rodríguez et al. 2016).

Table 1 *– continued*

Source ID	Target	RA	Dec.	Spec. type	Ref.
51	Cl∗ IC 348 LRL 241	03 44 59.83	+32 13 31.90	M4.5	1
52	Cl∗ IC 348 LRL 248	03 44 35.95	+32 09 24.31	M5.25	1
53	Cl∗ IC 348 LRL 256	03 43 55.27	+32 07 53.31	M5.75	1
54	Cl∗ IC 348 LRL 272	03 44 34.13	+32 16 35.77	M4.25	1
55	Cl∗ IC 348 LRL 276	03 44 09.21	+32 02 37.68	M0	1
56	Cl∗ IC 348 H 149	03 44 34.05	+32 06 57.05	M7.25	1
57	Cl∗ IC 348 LRL 292	03 43 59.87	+32 04 41.44	M5.75	1
58	Cl∗ IC 348 LRL 297	03 44 33.21	+32 12 57.46	M4.5	1
59	Cl∗ IC 348 LRL 300	03 44 38.97	+32 03 19.69	M5	1
60	Cl∗ IC 348 LRL 319	03 45 01.00	+32 12 22.21	M5.5	1
61	Cl∗ IC 348 LRL 324	03 44 45.22	+32 10 55.75	M5.75	1
62	Cl∗ IC 348 LRL 325	03 44 30.06	+32 08 48.90	M6	1
63	Cl∗ IC 348 LRL 334	03 44 26.66	+32 02 36.32	M5.75	1
64	Cl∗ IC 348 LRL 336	03 44 32.37	+32 03 27.48	M5.5	1
65	Cl∗ IC 348 LRL 341	03 44 12.98	+32 13 15.61	M5.25	1
66	Cl∗ IC 348 LRL 366	03 44 35.02	+32 08 57.34	M4.75	1
67	Cl∗ IC 348 LRL 382	03 44 30.96	+32 02 44.18	M5.5	1
68	Cl∗ IC 348 LRL 407	03 45 04.14	+32 05 04.38	M7	1
69	Cl∗ IC 348 LRL 415	03 44 29.97	+32 09 39.45	M6.5	1
70	2MASS J03444593+3203567	03 44 45.94	+32 03 56.78	M5.75	1
71	Cl∗ IC 348 LRL 462	03 44 24.46	+32 01 43.71	M3	1
72	Cl∗ IC 348 LRL 468	03 44 11.07	+32 01 43.60	M8.25	1
73	Cl∗ IC 348 LRL 555	03 44 41.22	+32 06 27.14	M5.75	1
74	Cl∗ IC 348 LRL 603	03 44 33.42	+32 10 31.50	M8.5	1
75	[PSZ2003] J034437.6+320832	03 44 37.64	+32 08 32.90	M5.5	1
76	[PSZ2003] J034426.4+320809	03 44 26.37	+32 08 09.94	M9	1
77	Cl∗ IC 348 LRL 690	03 44 36.38	+32 03 05.40	M8.75	1
78	Cl∗ IC 348 LRL 703	03 44 36.62	+32 03 44.20	M8	1
79	[PSZ2003] J034433.7+320521	03 44 33.70	+32 05 20.67	M6	1
80	[PSZ2003] J034433.7+320547	03 44 33.69	+32 05 46.71	M8.75	1
81	Cl∗ IC 348 LRL 746	03 44 49.96	+32 06 14.61	M5	1
82	[PSZ2003] J034419.7+320645	03 44 19.67	+32 06 45.93	M7	1
83	Cl∗ IC 348 LRL 2096	03 44 12.94	+32 13 24.06	M6	1
84	[PSZ2003] J034416.2+320540	03 44 16.18	+32 05 40.96	M9	1
85	Cl∗ IC 348 TJ 72	03 44 31.98	+32 11 43.95	G0	1
86	[BNM2013] 32.03 53	03 44 42.01	+32 08 59.98	M4.25	1
87	Cl∗ IC 348 LRL 8078	03 44 26.68	+32 08 20.35	M0.5	1
88	Cl∗ IC 348 LRL 9024	03 44 35.37	+32 07 36.24	M0	1
89	Cl∗ IC 348 H 110	03 44 25.58	+32 11 30.24	M2	1
90	2MASS J03452514+3209301	03 45 25.15	+32 09 30.18	M3.75	1
91	2MASS J03452046+3206344	03 45 20.46	+32 06 34.48	M1	1
92∗	Cl∗ IC 348 LRL 31	03 44 18.17	+32 04 57.04	G1	1
93∗	Cl∗ IC 348 LRL 329	03 44 15.58	+32 09 21.83	M7.5	1
94∗	Cl∗ IC 348 LRL 67	03 43 44.61	+32 08 17.76	M0.75	1
95	2MASS J03435856+3217275	03 43 58.57	+32 17 27.53	M3.5(IR)	2
96	Cl∗ IC 348 LRL 117	03 43 59.08	+32 14 21.31	M3.5(IR)	2
97	2MASS J03442724+3214209	03 44 27.25	+32 14 20.98	M3.5(IR)	2
98	2MASS J03434881+3215515	03 43 48.81	+32 15 51.55	M4.5(IR)	2
99	Cl∗ IC 348 LRL 179	03 44 34.99	+32 15 31.15	M3.5(IR)	2
100	Cl∗ IC 348 LRL 199	03 43 57.22	+32 01 33.90	M6.75(IR)	2
101	Cl∗ IC 348 LRL 215	03 44 28.95	+32 01 37.85	M3.25(IR)	2
102	2MASS J03443112+3218484	03 44 31.13	+32 18 48.49	M3.25(IR)	2
103∗	2MASS J03443468+3216000	03 44 34.69	+32 16 00.09	M3.5(IR)	2, 3
104	2MASS J03441522+3219421	03 44 15.22	+32 19 42.18	M4.75(IR)	2
105	2MASS J03442294+3214404	03 44 22.94	+32 14 40.43	M5.5(IR)	2
106	2MASS J03440599+3215321	03 44 05.99	+32 15 32.15	M6.5(IR)	2
107	Cl∗ IC 348 LRL 364	03 44 43.01	+32 15 59.67	M4.75(IR)	2
108	Cl∗ IC 348 LRL 368	03 44 25.70	+32 15 49.27	M5.5(IR)	2
109	Cl∗ IC 348 LRL 406	03 43 46.44	+32 11 05.94	M5.75(IR)	2
110	2MASS J03445853+3158270	03 44 58.54	+31 58 27.03	M6.5(IR)	2

Table 1 – *continued*

Source ID	Target	RA	Dec.	Spec. type	Ref.
111	2MASS J03432845+3205058	03 43 28.45	+32 05 05.82	M4(IR)	2
112	Cl∗ IC 348 LRL 753	03 44 57.62	+32 06 31.25	XXX	2
113	2MASS J03445688+3220355	03 44 56.88	+32 20 35.52	M6(IR)	2
114	Cl∗ IC 348 LRL 1379	03 44 52.00	+31 59 21.50	M9.75	2
115	2MASS J03445205+3158252	03 44 52.06	+31 58 25.21	M3.5(IR)	2
116	Cl∗ IC 348 LRL 1683	03 44 15.83	+31 59 36.77	M5.25(IR)	2
117	Cl∗ IC 348 LRL 1707	03 43 47.64	+32 09 02.56	M7(IR)	2
118	2MASS J03451307+3220053	03 45 13.07	+32 20 05.32	M5(IR)	2
119	2MASS J03442721+3220288	03 44 27.21	+32 20 28.82	M5(IR)	2
120	2MASS J03435056+3203180	03 43 50.57	+32 03 18.00	M8.75(IR)	2
121	Cl∗ IC 348 LRL 1881	03 44 33.79	+31 58 30.28	M3.75(IR)	2
122	2MASS J03432355+3212258	03 43 23.56	+32 12 25.82	M4.5(op)	2
123	V∗ V338 Per	03 43 28.20	+32 01 59.12	M1.75(IR)	2
124	Cl∗ IC 348 LRL 1923	03 44 00.47	+32 04 32.71	M5(IR)	2
125	Cl∗ IC 348 LRL 1925	03 44 05.77	+32 00 01.10	M5.5(IR)	2
126	EM∗ LkHA 99	03 45 16.35	+32 06 19.95	K5(op)	2
127	2MASS J03445997+3222328	03 44 59.98	+32 22 32.83	M5.25	2
128	2MASS J03451782+3212058	03 45 17.83	+32 12 05.85	M3.75(op)	2
129	2MASS J03431581+3210455	03 43 15.81	+32 10 45.53	M4.5(IR)	2
130	2MASS J03453563+3159544	03 45 35.64	+31 59 54.44	M4.5(IR)	2
131	2MASS J03452212+3205450	03 45 22.13	+32 05 45.01	M8(IR)	2
132	2MASS J03442186+3217273	03 44 21.86	+32 17 27.31	M4.75(op)	2
133	Cl∗ IC 348 LRL 22865	03 45 17.65	+32 07 55.33	L0	2
134	Cl∗ IC 348 LRL 40182	03 45 03.83	+32 00 23.30	–	2
135	Cl∗ IC 348 LRL 54299	03 43 44.27	+32 03 42.60	–	2
136	2MASS J03451349+3224347	03 45 13.50	+32 24 34.71	M4.25	2

Ref.: (1) Lada et al. (2006), (2) Muench et al. (2007), (3) Espaillat et al. (2012).
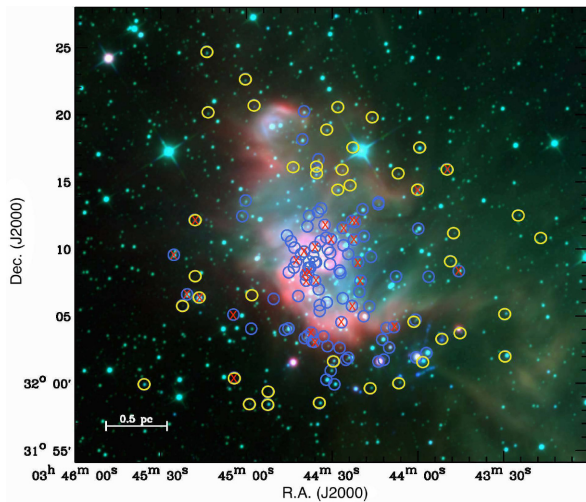∗ Transitional disc

Figure 2. IR map of IC 348 star-forming region with our ALMA targets. ALLWISE three-colour image with RGB mapped to 22 (W4), 4.6 (W2), and 3.4 (W1) μm. Yellow and blue circles correspond to the sample selected from Muench et al. (2007) and Lada et al. (2006), respectively. Red crosses indicate the positions of IC 348 members used to estimate a mean cluster distance of 310 pc ± 20 pc, based on the *Gaia* DR2 parallax data.

3 ALMA OBSERVATIONS AND DATA REDUCTION

ALMA observations towards our IC 348 targets were carried out in Band 6 (211–275 GHz) under the project code: 2015.1.01037.S. Our science goal was executed in Cycle 3 with the C40-4 array configuration and was observed between the 2015 June 23 and 2015

June 27. The Band 6 continuum observations were conducted with a total on-source integration time of ∼1 min per target over three execution blocks, each one targeting all 136 objects for 0.3 min. The adopted setup included two spectral windows for continuum observations with effective bandwidths of 1.875 GHz centred at 218.0 and 233.0 GHz, for a mean frequency of 225.676 GHz (∼1.3 mm). The typical (1σ) noise level reached is ∼0.15 mJy beam^{-1}. We also targeted molecular emission lines of ^{12}CO, ^{13}CO, and C^{18}O (J = 2−1), centred on 230.535, 220.395, and 219.557 GHz, respectively. Each line was observed with a resolution of 242 kHz (0.3 km s^{-1}) and a bandwidth of 117.2 MHz. The ALMA data were reduced using the Common Astronomy Software Application (CASA) package, version 4.5.3 (McMullin et al. 2007). Initial calibration (i.e. water vapour radiometer corrections, phase and amplitude calibrations) was performed by the ALMA science operations team during quality assurance. The flux calibrator was J0237+2848. J0238+1636 and J0336+3218 were chosen as bandpass calibrators and J0510+1800 as a phase calibrator. To reach the requested synthesized beam size of ∼0.8 arcsec, we applied the CLEAN algorithm to the calibrated visibilities and extracted the continuum images by applying a Briggs weighting with a robust parameter of +2, which is close to a natural weighting. Using the *uvcontsub* routine, we subtracted the continuum emission from the spectral windows to extract the ^{12}CO, ^{13}CO, and C^{18}O spectral line data from the calibrated visibilities.

4 RESULTS

4.1 Detection criteria

We searched for 1.3 mm continuum emission centred on the 2MASS positions of the 136 targets, listed in Table 1. From the continuum

images, we determined the peak flux and rms using the task *imstat* and thus estimated the signal to noise (S/N, ratio between peak and rms) ratio for each image. Peak fluxes were derived from a 4 arcsec radius circle, and the rms from a 4–7 arcsec radius annulus centred on the expected source position. A source with S/N < 4 is considered a non-detection. For these sources, we measured the flux densities using the *uvmodelfit* routine in CASA and fitting a point source in the UV-plane. If the flux density is less than 4σ, the point source fit is applied to the visibilities with the pointing centre as a free parameter. If the flux density is less than 3σ, it is fit with a point source with the offset position fixed. Table 2 lists integrated flux density ($F_{1.3\,\mathrm{mm}}$) and rms for non-detected sources.

For detections (S/N > 4), flux densities were measured by applying an elliptical Gaussian model to the visibility data using *uvmodelfit* in CASA. This model is centred at the nominal source position and provides the parameters $F_{1.3\,\mathrm{mm}}$, the full width at half-maximum (FWHM) along the major axis, aspect ratio, position angle of the major axis (PA), and coordinate offsets ($\Delta\alpha$ and $\Delta\delta$). These parameters are listed in Table 3. A disadvantage of fitting the brightness profile of a source in the ultraviolet (UV)-plane directly is the possibility of including emission from a second source in the fitting process. To avoid any contamination in the measured flux of each field, we visually inspected the image plane for pixels with significant brightness ($>4\sigma$). Applying these methods, we detect 40 of the 136 IC 348 targets at $>4\sigma$ significance. Images of the 40 sources are displayed in Fig. 3. We find that 10 of the targets are partially resolved, giving PA values with large uncertainties, and therefore, we do not report those values here. For these objects, the source sizes (deconvolved from the beam) are listed in Table 3.

Using standard approaches (e.g. Hildebrand 1983), the mm flux can be translated into a disc mass according

$$M_{dust} = \frac{F_{\nu} d^2}{\kappa_{\nu} B_{\nu}(T_{dust})}, \quad (1)$$

where F_{ν} is the integrated flux, d is the distance to the target, $B_{\nu}(T_{\mathrm{dust}})$ is the Planck function at the average disc temperature, and κ_{ν} is the total opacity. Thus, adopting a distance of 310 pc (Section 4.2) and making standard assumptions concerning the disc temperature ($T_{\mathrm{dust}} = 20\mathrm{K}$) and dust opacity ($\kappa_{\nu} = 2.3\ \mathrm{cm}^2\mathrm{g}^{-1}$ at 1.33 mm; Andrews & Williams 2005, and references therein), we estimate disc masses for all detected targets and report them in Table 3.

Similarly, the 3σ upper limits of ~ 0.45 mJy for most of our targets correspond to a dust mass of $M_{\mathrm{Dust}} \sim 1.3\ M_{\oplus}$.

4.2 Target properties

Most of our ALMA targets have fundamental stellar parameters, such as extinction, stellar masses, luminosity, effective temperature, etc., reported in previous studies. However, not all values have been obtained in homogeneous manner, and uncertainties might be larger due to systematic differences in methodology or the adopted distance to IC 348. Considering that the most recent data releases of the *Gaia* DR2 and Pan-STARRS-1 (PS1) are available, we seek for uniformity in these estimations. We adopt a uniform distance of 310 ± 20 pc to all targets based on the *Gaia* DR2 parallax measurements (Luri et al. 2018) of 35 targets in our sample that have DR2 parallax uncertainties smaller than 10 per cent. These objects are indicated with red crosses in Fig. 2. To estimate the visual extinction (A_v), we use the extinction relations $\frac{A_{\lambda_{\mathrm{eff}}}}{A_v}$ listed in Table 4, which are calculated using the extinction law presented in Cardelli, Clayton & Mathis (1989). We use PS1 colours $r-z$ and $z-y$

(Magnier et al. 2013), in order of preference, and adopt the relations $A_z = 1.4[(r - z) - (r - z)_0]$ and $A_y = 6.3[(z - y) - (z - y)_0]$, where $(r - z)_0$ and $(z - y)_0$ are the expected PS1 colours of a main-sequence star generated from MARCS synthetic fluxes (Gustafsson et al. 2008). In the special case of Class II objects lacking PS1 photometry in the necessary bands, we adopted A_v from Currie & Kenyon (2009).

The stellar luminosities ($L_{\star}$) of IC 348 members are calculated via the dereddened J-band photometry method of Kenyon & Hartmann (1995) and adopting the distance of 310 pc. We derived the stellar properties based on the spectral types taken from Luhman et al. (2003) and Muench et al. (2007) and a conversion from spectral type to the effective temperature (T_{eff}) taken from Pecaut & Mamajek (2013) with uncertainties of ± 1 spectral subclass (Table 5). Using T_{eff} and $L_{\star}$, and assuming all targets are single star systems, we estimated the stellar masses ($M_{\star}$) and ages from comparisons with theoretical pre-main-sequence (PMS) evolutionary tracks. Masses and ages of targets with stellar masses between 0.01 and 1.4 $M_{\odot}$ were derived from the models presented in Baraffe et al. (2015) and stellar masses $>1.4 M_{\odot}$ from the PARSEC evolutionary models (Bressan et al. 2012). Age uncertainties are based mainly on the H–R diagram placement and the determination of $L_{\star}$, incorporating the estimated observational photometry, J-band bolometric correction, and extinction uncertainties. Nevertheless, the dominant sources of error on the $L_{\star}$ values are the ~ 10 per cent distance and extinction uncertainties (Cieza et al. 2007). Stellar mass uncertainties are dominated by the ± 1 spectral subclass and determined by their spectral type. For these T Tauri stars, whose metallicity values are unknown, we adopted solar composition, and we held the surface gravity fixed at the value log g = 4.0, typical for PMS stars. Table 5 lists the resulting adopted T_{eff}, estimated stellar age, A_v, $L_{\star}$, and estimated stellar mass of these objects. Fig. 4 shows Baraffe evolutionary models with our IC 348 target selection. The stars are clustered around the 2–3Myr isochrones, in agreement with previous age estimates for the region.

In Figure 5, we plot the SEDs of all targets detected at 1.3 mm, including photometry from PS1 (0.48, 0.62, 0.75, 0.87, and 0.96 μm), 2MASS (1.25, 1.65, and 2.22 μm) and Spitzer/IRAC (3.6, 4.5, 5.8, 8, and 24 μm, Skrutskie et al. 2006; Evans et al. 2003; Currie & Kenyon 2009). The photometric data were dereddened using the Mathis & Cardelli (1990) approach. To calculate the stellar synthetic photometry with a fixed temperature $T_{\star}$, which is approximated by T_{eff}, we interpolated the response curves for the set of filters used in the fitting, and used the BT-Settl spectral models for the corresponding $T_{\star}$ (Allard 2014). Then, we convolved the filter response curves with the synthetic spectra, to match the spectral resolution. Because the PS1, 2MASS, IRAC, and 24 μm data have photometric uncertainties between a few per cent and 0.1 mag for the objects investigated here, systematic effects can contribute up to 0.1 mag. To account for flux variability of the objects, we added an observational error of 15 per cent. A multiplicative dilution factor, $\left(\frac{R_{\star}}{d}\right)^2$, relating the central star radius ($R_{\star}$) and the distance to the object (d) is used to normalize the optical bands.

In Fig. 6, we plot mm flux as a function of stellar mass. The 8 transition discs in our sample are indicated as red symbols. Some of these objects are among the most massive discs in the cluster, with disc masses of several M_{Jup}, assuming a standard gas to dust mass ratio of 100. In particular, three of the six brightest discs in the entire sample are transition objects based on their SEDs (Cl∗ IC 348 LRL 31, Cl∗ IC 348 LRL 67, and 2MASS J03443468+3216000), a trend that was already reported by Cieza et al. (2015) based on shallower SCUBA-2 observations of the cluster at 850 μm.

Table 2. Non-Detected Class II Sources in IC 348.

Source	$F_{1.3\,mm}$ [mJy]	rms [mJy beam^{-1}]	Source	$F_{1.3\,mm}$ [mJy]	rms [mJy beam^{-1}]
1	0.19 ± 0.13	0.14	71	0.35 ± 0.13	0.13
2	0.51 ± 0.13	0.13	72	0.06 ± 0.13	0.13
5	0.31 ± 0.15	0.13	73	0.40 ± 0.14	0.13
6	0.52 ± 0.15	0.13	74	0.04 ± 0.13	0.14
8	0.01 ± 0.14	0.14	75	0.30 ± 0.14	0.13
12	-0.07 ± 0.14	0.14	76	-0.02 ± 0.14	0.14
16	-0.05 ± 0.14	0.14	77	-0.19 ± 0.15	0.14
18	0.17 ± 0.13	0.12	78	0.08 ± 0.14	0.13
19	0.06 ± 0.15	0.13	79	0.36 ± 0.13	0.14
21	0.04 ± 0.14	0.14	80	0.27 ± 0.13	0.14
22	0.12 ± 0.13	0.13	81	0.08 ± 0.13	0.14
23	-0.09 ± 0.14	0.14	82	-0.11 ± 0.13	0.13
24	0.13 ± 0.12	0.13	83	0.20 ± 0.14	0.13
26	0.41 ± 0.14	0.14	84	0.09 ± 0.13	0.13
27	-0.42 ± 0.13	0.14	85	0.26 ± 0.13	0.15
28	-0.15 ± 0.13	0.14	89	0.49 ± 0.14	0.14
29	0.15 ± 0.15	0.14	93	0.26 ± 0.13	0.14
30	0.26 ± 0.15	0.14	97	0.32 ± 0.14	0.12
31	0.03 ± 0.13	0.14	98	0.16 ± 0.13	0.13
32	0.36 ± 0.14	0.13	99	0.25 ± 0.14	0.14
33	0.16 ± 0.15	0.13	100	0.41 ± 0.15	0.13
37	0.02 ± 0.12	0.14	104	0.16 ± 0.13	0.13
39	0.37 ± 0.15	0.13	105	0.21 ± 0.13	0.14
40	0.31 ± 0.14	0.14	106	0.24 ± 0.12	0.13
42	0.16 ± 0.13	0.14	107	0.38 ± 0.14	0.13
44	0.19 ± 0.13	0.14	108	0.36 ± 0.14	0.13
45	0.35 ± 0.14	0.14	109	-0.31 ± 0.13	0.12
46	0.24 ± 0.13	0.14	110	0.14 ± 0.14	0.14
47	-0.13 ± 0.13	0.14	112	-0.38 ± 0.14	0.13
49	-0.13 ± 0.13	0.14	113	0.21 ± 0.14	0.13
50	0.20 ± 0.13	0.13	114	0.05 ± 0.13	0.12
51	0.05 ± 0.13	0.13	115	0.03 ± 0.13	0.13
53	0.09 ± 0.13	0.13	117	0.25 ± 0.14	0.13
54	0.50 ± 0.13	0.13	118	0.28 ± 0.14	0.15
56	0.04 ± 0.14	0.14	119	0.35 ± 0.13	0.14
57	0.33 ± 0.14	0.13	120	-0.44 ± 0.17	0.19
58	0.15 ± 0.12	0.13	122	0.02 ± 0.12	0.13
59	-0.28 ± 0.13	0.14	123	0.21 ± 0.13	0.14
60	0.20 ± 0.17	0.16	124	0.36 ± 0.13	0.14
61	-0.18 ± 0.13	0.14	125	0.15 ± 0.14	0.13
62	0.24 ± 0.12	0.13	127	-0.06 ± 0.15	0.14
63	0.17 ± 0.14	0.12	128	-0.04 ± 0.13	0.14
64	0.14 ± 0.13	0.14	130	0.32 ± 0.13	0.13
65	0.02 ± 0.14	0.14	131	-0.08 ± 0.14	0.14
66	-0.18 ± 0.13	0.14	133	0.05 ± 0.13	0.13
68	0.45 ± 0.15	0.13	134	-0.06 ± 0.12	0.15
69	0.37 ± 0.13	0.14	135	0.07 ± 0.13	0.13
70	0.15 ± 0.14	0.14	136	0.18 ± 0.14	0.14

Three transition discs (Cl∗ IC 348 LRL 97∗, Cl∗ IC 348 LRL 229∗, and Cl∗ IC 348 LRL 329) remained undetected. These results fit well in the scenario proposed by Owen & Clarke (2012) and Cieza et al. (2012), in which there are at least two types of transition discs with inner opacity cavities that are the result of distinct processes: (1) gas-accreting transition discs that are massive and have large inner holes caused by the formation of giant planets, (multiple) lower mass planets, or subsequent migration (van der Marel et al. 2018), and (2) non-accreting transition objects with low disc masses that have inner holes carved by photoevapouration during the final stages of disc dissipation.

5 DISCUSSION

5.1 Non-detections

The ensemble of undetected sources can be used to estimate the typical disc mass of the faint sources in IC 348. Initially, we stacked different spectral type sub-groups of these non-detections to constrain their average properties. We do not obtain significant detections in stacked images. Therefore, we stacked the 96 non-detections, after centreing each field on the expected stellar position to create an average image that has noise that is a factor of ∼7 lower than in the individual fields. After doing so, we find a clear signal of

Table 3. Continuum detections of Class II sources in IC 348.

Source	$F_{1.3\,mm}$* (mJy)	rms (mJy beam^{-1})	$\Delta\alpha$ (arcsec)	$\Delta\delta$ (arcsec)	a (arcsec)	M_{Dust} ($M_\oplus$)
3	2.50 ± 0.24	0.14	0.19	−0.16	0	6.99 ± 0.30
4	1.28 ± 0.15	0.13	0.06	−0.13	0	3.58 ± 0.28
7	5.68 ± 0.45	0.13	−0.09	−0.08	0	15.88 ± 0.28
9	0.70 ± 0.14	0.13	−0.02	−0.10	0	1.96 ± 0.28
10	3.23 ± 0.29	0.14	0.12	−0.06	0	9.03 ± 0.30
11	0.96 ± 0.14	0.13	0.11	−0.12	0	2.68 ± 0.28
13	54.18 ± 4.41	0.27	0.14	0.03	0.21 ± 0.01	151.82 ± 0.57
14	0.78 ± 0.22	0.13	−0.02	−0.14	0	2.18 ± 0.28
15	2.24 ± 0.22	0.14	−0.13	−0.08	0	6.26 ± 0.30
17	1.55 ± 0.17	0.14	0.07	−0.04	0	4.33 ± 0.30
20	0.78 ± 0.15	0.13	−0.34	−0.40	0	2.18 ± 0.28
25	1.22 ± 0.17	0.13	0.01	−0.20	0	3.41 ± 0.28
34	4.09 ± 0.36	0.13	−0.14	−0.28	0.23 ± 0.04	11.43 ± 0.28
35	6.34 ± 0.54	0.13	−0.01	−0.15	0.33 ± 0.02	17.72 ± 0.28
36	1.74 ± 0.20	0.14	−0.09	−0.13	0	4.86 ± 0.30
38	1.42 ± 0.17	0.13	−0.23	−0.25	0	3.97 ± 0.28
41	0.61 ± 0.13	0.13	0.17	0.18	0	1.70 ± 0.28
43	0.59 ± 0.14	0.14	−0.06	−0.06	0	1.65 ± 0.30
48	2.08 ± 0.2	0.13	0.10	−0.03	0	5.81 ± 0.28
52	0.67 ± 0.14	0.14	0.10	−0.04	0	1.87 ± 0.30
55	0.80 ± 0.15	0.14	0.10	−0.17	0	2.24 ± 0.30
67	1.91 ± 0.21	0.13	0.13	−0.04	0	5.34 ± 0.28
86	1.27 ± 0.17	0.13	−0.10	−0.31	0	3.55 ± 0.28
87	0.70 ± 0.14	0.13	−0.02	−0.13	0	1.96 ± 0.28
88	2.99 ± 0.28	0.13	−0.02	−0.03	0	8.36 ± 0.28
90	1.69 ± 0.20	0.15	0.11	−0.08	0.37 ± 0.08	4.72 ± 0.32
91	6.73 ± 0.58	0.15	0.08	−0.17	0.38 ± 0.02	18.81 ± 0.32
92	12.01 ± 1.12	0.16	0.09	−0.09	0.47 ± 0.01	33.57 ± 0.34
94	6.00 ± 0.50	0.14	0.05	−0.27	0.31 ± 0.02	16.77 ± 0.30
95	1.88 ± 0.22	0.14	0.09	−0.26	0	5.25 ± 0.30
96	1.76 ± 0.19	0.14	0.10	−0.10	0	4.92 ± 0.30
101	2.50 ± 0.24	0.14	−0.01	−0.06	0	6.99 ± 0.30
102	0.73 ± 0.14	0.14	0.20	0.01	0	2.04 ± 0.30
103	7.22 ± 0.58	0.14	0.02	−0.06	0.30 ± 0.02	20.18 ± 0.30
111	1.06 ± 0.16	0.13	−0.02	−0.01	0	2.96 ± 0.28
116	1.43 ± 0.16	0.13	0.04	−0.08	0	4.03 ± 0.28
121	4.83 ± 0.41	0.14	0.11	0	0.22 ± 0.04	13.50 ± 0.30
126	6.54 ± 0.52	0.13	0	−0.04	0	18.28 ± 0.28
129	0.62 ± 0.15	0.12	0.18	−0.29	0.39 ± 0.17	1.73 ± 0.25
132	1.05 ± 0.15	0.13	0.17	−0.17	0	2.93 ± 0.28

*The elliptical Gaussian model applied to the resolved sources generates five free parameters. Here, we report: integrated flux density ($F_{1.33mm}$), FWHM along the major axis (a), right ascension offset from the phase centre ($\Delta\alpha$), and declination offset from the phase centre ($\Delta\delta$).

0.14 ± 0.02 mJy (Fig. 7), indicating that there are many targets in IC 348 with fluxes very close to the 1σ noise of our observations. The 0.14 mJy flux measurement resulting from the stacking exercise suggests that the average dust mass of the discs that were not individually detected is only ∼0.40 $M_\oplus$. This implies that, for most discs in the IC 348 cluster, the amount of mm-sized dust that is still available for planet formation is of the order of the mass of the planet Mars. *Kepler* has recently found that M-type stars host an average of 2.2 ±0.3 planets with radii of ∼1 $R_\oplus$ and orbital periods of 1.5 to 180 days (Gaidos et al. 2016);

therefore, it is expected that most stars in IC 348 should form multiple rocky planets even though most of the cluster members have already lost their discs (within the stringent limits imposed by the infrared observations) or have very little dust left. Thus, we conclude that most discs around IC 348 members contain several Earth masses worth of solids in bodies that are at least several cm in size i.e. large enough to become undetectable by ALMA

observations. More significantly, this suggests that these protoplanetary discs are likely sites of recently formed planetary systems like our own. In addition, IR emission from discs not detected at mm wavelengths connotes the existence of small, optically thick discs with extensions of <1 au. Our observations also constrain the amount of second-generation dust produced in the systems not detected by ALMA to be <0.4 $M_\oplus$, which still leaves significant room to explain the observed IR excesses. In fact, a small amount of warm grains of micron sizes (<1 lunar mass) is sufficient to produce the observed excesses at 10 μm (e.g. Nagel et al. 2010).

In addition, our survey RMS of ∼0.15 mJy results in a large number of non-detections with respect to other surveys, mainly because of a lower sensitivity at late spectral types (M4-M9) at a distance of 310 pc. Detecting such late M stars individually (with S/N of >4) at 1.3 mm would require 10× our exposure time. However, we note that objects with a disc mass of ∼1 $M_\oplus$ are individually
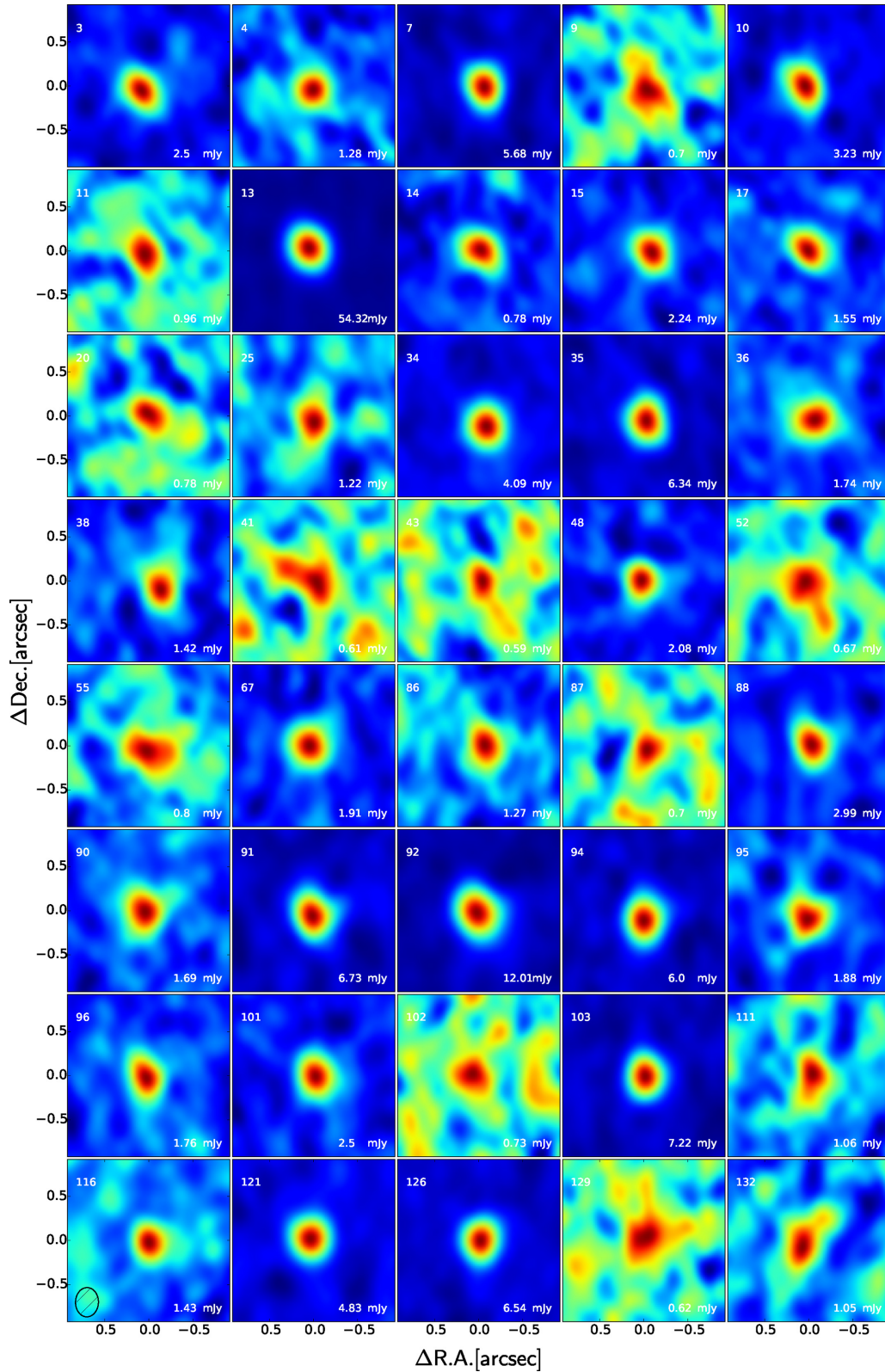
Figure 3. 1.3 mm continuum images meeting our detection criteria (>4σ) in the IC 348 region, see Section 4.1. Each image covers 1.7 arcsec × 1.7 arcsec size with an average beam size of 0.8 arcsec × 0.7 arcsec. Integrated flux density values are presented at the low-right corner as reported in Table 3.

detected with an S/N of ∼10 in the Lupus survey because of the much smaller (150 pc) distance of some of the Lupus PMS stars and, to a lesser extent, the use of a shorter observing wavelength

(Ansdell et al. 2016). This implies that at a distance of 150 pc and a sensitivity of 0.45 mJy in Band 6, it should possible to detect discs with dust masses of only ∼0.26 $M_\oplus$.

Table 4. Extinction relations calculated following the Cardelli et al. (1989) extinct law with $R_v = 3.1$.

Filter ID	$A_{\lambda_{eff}}$ (Å)	$\frac{A_{\lambda_{eff}}}{A_v}$	Zero point (Jy)
g	4775.6	1.19	3631
r	6129.5	0.89	3631
i	7484.6	0.67	3631
z	8657.8	0.51	3631
y	9603.1	0.44	3631

5.2 Disc evolution

Disc properties determine possible planet-formation scenarios. Investigating basic disc parameters such as mass and size at different evolutionary stages is thus vital for planet-formation theory. Nearby star-forming regions such as Taurus (1–3 Myr), Lupus (1–3 Myr), Cha I (2–3 Myr), σ Ori (3–5 Myr), and Upper Scorpius (5–10 Myr) are ideal targets to track evolutionary patterns because the ages of these populations cover the disc dispersal time-scale. Recently, (sub-)mm continuum flux surveys of these star-forming regions have shown that disc masses decline with age and that there is a strong dependence of mm-wavelength luminosity on stellar mass (Andrews et al. 2013; Ansdell et al. 2016, 2017; Barenfeld et al. 2016; Pascucci et al. 2016). Therefore, in order to compare IC 348 to other regions and investigate the evolution of disc masses as a function of stellar age, we need to take into account that disc masses and mm detection rates depend on spectral types and stellar mass. Fig. 8 displays the distribution of stellar spectral types for the detected and non-detected sources, showing the low detection rate at later spectral types (Tables 2 and 3).

Because estimates of stellar masses depend sensitively on inputs such as distances and theoretical models, here we used the statistical methodology presented in Andrews et al. (2013) based on spectral types. While solar-mass stars evolve in spectral types during PMS stages, lower mass stars (0.1–0.7 M$_\odot$) evolve at almost constant temperature for the first ∼10 Myr (see evolutionary models in Fig. 4). This supports the use of spectral types as a proxy for stellar mass in the mass range of the stars in our IC 348 sample. Hence, to statistically compare samples from different regions, we perform Monte Carlo simulations, whose 'reference' sample is IC 348, while a 'comparison' sample can be Taurus, Chamaeleon I, Lupus, Upper Scorpius, or σ Ori. The 'comparison' sample is appropriately scaled to the IC 348 distance (310 pc) and modified for the respective observing wavelengths using the mean (sub-)mm flux ratios observed in Taurus ($F_\lambda = F_{1.3mm} \times (1.3mm/\lambda)^{2.5}$). Upper limit inputs for the 'comparison' samples are as reported in the literature: three times the rms noise of the observations for Taurus, Lupus, Cha I, and Orionis, while the upper limits in Upper Scorpius are given by three times the rms noise plus any positive measured flux density. To construct our simulations, we first define a set of spectral type bins ranging from A2 to M6, corresponding to the distribution of the IC 348 sample, and place the comparison objects in those bins. Then, disc mm-wave luminosities are randomly drawn from the reference region (IC 348) in each of these spectral type bins, such that the reference and comparison samples have the same spectral type distributions. In this manner, we simulate 10^6 synthetic 'reference' disc ensembles that are used to construct Cumulative Distribution Functions (CDF); see Fig. 9. Each of these CDFs is compared to the comparison sample to estimate the probability that the two distributions are drawn from the same parent population using a censored statistical test (i.e the Gehan test;

Feigelson & Nelson 1985). The result is a list of 10^6 such probabilities for each comparison region. The cumulative distributions for these probabilities, $f(p_\phi)$, are also shown in Fig. 9 (bottom-right panel).

5.2.1 Relative flux densities

The CDFs for the scaled flux densities show that the discs orbiting IC 348 stars are fainter on average than discs in Taurus, Lupus, Cham I, and σ Ori. Cieza et al. (2015) presented a similar statistical analysis based on shallower SCUBA-2 observations of IC 348 and found that the fluxes in this cluster were slightly lower than in Taurus. Here, we confirm that the fluxes in IC 348 are ∼4× fainter than in Taurus with a very high level of significance: virtually all 10^6 tests indicate that the probability that disc luminosities in Taurus and IC 348 are drawn from the same parent population is $<10^{-12}$. Similarly, we find that the younger Lupus region has a substantially brighter distribution compared to the older IC 348 region, at the $\gtrsim 3\sigma$ level. The difference between the luminosity distributions of IC 348 and Cha I is marginal, with IC 348 being slightly fainter than Cha I, while, the luminosity distributions of σ Ori and IC 348 are statistically indistinguishable ($\lesssim 2\sigma$). In addition, Upper Scorpius is also very different from IC 348 (all tests indicate differences $>3\sigma$), but in the opposite sense: the Upper Scorpius discs are fainter than discs in IC 348, which reflects the fact that the mean dust mass is lower at the 5–10 Myr age of Upper Scorpius. In summary, these mm observations trace the population of mm/centimeter-sized grains at radial distances >10 au, confirming a significant dispersal process in the outer disc over a time-scale of ∼1−10Myr.

Infrared surveys with the *Spitzer Space Telescope*, at IRAC wavelengths (3.6−4.5 μm), previously established that the fraction of optically thick dust disc decreases with age, yielding disc fractions (per cent) of 63 ± 4 in Taurus, 52 ± 5 in Lupus, 52 ± 6 in Cha I, 39 ± 6 in σ Ori, 36 ± 3 in IC 348, and only 16 ± 6 in Upper Scorpius (Ribas et al. 2014). These IR observations probe the dispersion of micron-sized grains within a few au (<10 au) from the central star. While IR discs observations are very sensitive and typically less biased with respect to spectral type, (sub-)mm detection rates are much lower and usually very biased against the lower end of the stellar mass function (M4–M9), making the interpretation of the results difficult.

5.2.2 Continuum luminosity distributions

Fig. 9 (bottom-right panel) compares the disc luminosity distributions of the 'comparison' and 'reference' samples, where p_ϕ is the probability that the two distributions are drawn from the same parent population and the vertical green bars indicate the nominal 2σ, 3σ, and 4σ probabilities. The cumulative distributions derived from the the Peto-Prentice test indicate medians of $p_\phi = 2.3 \times 10^{-12}$ and 5.5×10^{-9} for Taurus and Upper Scorpius, respectively, implying a $> \times 4\sigma$ difference. The Lupus and Cha I samples appear to have a difference of $\gtrsim 3\sigma$ in their luminosity distributions, as indicated by medians of $p_\phi = 1.7 \times 10^{-3}$ and $p_\phi = 4.7 \times 10^{-3}$, respectively. Meanwhile, the σ Ori has a luminosity distribution that is statistically indistinguishable ($\lesssim 2\sigma$) from the IC 348 sample, with $p_\phi = 1.1 \times 10^{-1}$.

It is noteworthy that the disc luminosity distribution of our IC 348 sample is significantly different from those of the Taurus and Upper Scorpius samples. As mentioned above, IC 348 is

Table 5. Stellar properties for Class II sources in IC 348.

Source ID	Log T_{eff} (K)	A_v (mag)	Log $L_\star$ ($L_\odot$)	$M_\star$ ($M_\odot$)	Source ID	Log T_{eff} (K)	A_v (mag)	Log $L_\star$ ($L_\odot$)	$M_\star$ ($M_\odot$)
1	$3.95^{+0.02}_{-0.01}$	2.87 ± 0.08	$2.00^{+0.16}_{-0.19}$	$3.17^{+0.00}_{-0.00}$	69	$3.45^{+0.01}_{-0.02}$	2.85 ± 0.16	$-1.70^{+0.24}_{-0.38}$	$0.04^{+0.01}_{-0.01}$
2	$3.72^{+0.01}_{-0.01}$	4.60 ± 0.03	$0.85^{+0.17}_{-0.21}$	$1.80^{+0.00}_{-0.00}$	70	$3.45^{+0.01}_{-0.02}$	4.18 ± 0.11	$-1.55^{+0.24}_{-0.38}$	$0.05^{+0.01}_{-0.01}$
3	$3.58^{+0.01}_{-0.02}$	13.93 ± 1.89	$0.36^{+0.20}_{-0.26}$	$0.47^{+0.03}_{-0.04}$	71	$3.53^{+0.02}_{-0.03}$	9.34 ± 0.24	$-1.18^{+0.24}_{-0.33}$	$0.30^{+0.05}_{-0.07}$
4	$3.58^{+0.01}_{-0.01}$	2.22 ± 0.03	$0.04^{+0.23}_{-0.30}$	$0.48^{+0.03}_{-0.04}$	72	$3.41^{+0.01}_{-0.02}$	4.38 ± 0.49	$-2.20^{+0.27}_{-0.93}$	$0.02^{+0.01}_{-0.01}$
5	$3.95^{+0.02}_{-0.01}$	1.30 ± 0.01	$1.08^{+0.16}_{-0.19}$	$1.89^{+0.00}_{-0.00}$	73	$3.45^{+0.01}_{-0.02}$	1.70 ± 0.08	$-1.48^{+0.24}_{-0.38}$	$0.05^{+0.01}_{-0.01}$
6	$3.60^{+0.01}_{-0.00}$	8.99 ± 0.36	$0.30^{+0.18}_{-0.20}$	$0.60^{+0.02}_{-0.01}$	74	$3.41^{+0.01}_{-0.02}$	4.11 ± 0.89	$-2.22^{+0.27}_{-0.93}$	$0.02^{+0.01}_{-0.01}$
7	$3.60^{+0.01}_{-0.00}$	3.60 ± 0.06	$-0.06^{+0.19}_{-0.21}$	$0.61^{+0.02}_{-0.01}$	75	$3.46^{+0.04}_{-0.01}$	5.40 ± 0.10	$-2.89^{+0.20}_{-0.19}$	$0.07^{+0.04}_{-0.01}$
8	$3.60^{+0.01}_{-0.01}$	2.52 ± 0.06	$0.04^{+0.21}_{-0.22}$	$0.65^{+0.05}_{-0.02}$	76	$3.39^{+0.00}_{-0.00}$	1.60 ± 0.10	$-2.98^{+0.16}_{-0.19}$	$0.02^{+0.01}_{-0.01}$
9	$3.60^{+0.01}_{-0.01}$	2.32 ± 0.12	$-0.09^{+0.21}_{-0.22}$	$0.69^{+0.05}_{-0.02}$	77	$3.39^{+0.02}_{-0.00}$	4.39 ± 0.53	$-2.06^{+0.26}_{-1.03}$	$0.01^{+0.01}_{-0.01}$
10	$3.60^{+0.00}_{-0.01}$	2.67 ± 0.09	$-0.25^{+0.17}_{-0.24}$	$0.61^{+0.01}_{-0.02}$	78	$3.41^{+0.01}_{-0.02}$	3.87 ± 0.34	$-1.43^{+0.27}_{-0.94}$	$0.03^{+0.01}_{-0.10}$
11	$3.60^{+0.01}_{-0.00}$	3.94 ± 0.12	$-0.34^{+0.19}_{-0.21}$	$0.69^{+0.02}_{-0.01}$	79	$3.45^{+0.00}_{-0.00}$	1.60 ± 0.10	$-3.01^{+0.16}_{-0.19}$	$0.06^{+0.00}_{-0.00}$
12	$3.58^{+0.01}_{-0.02}$	9.44 ± 0.07	$0.13^{+0.20}_{-0.26}$	$0.45^{+0.03}_{-0.04}$	80	$3.39^{+0.00}_{-0.00}$	1.50 ± 0.10	$-2.73^{+0.16}_{-0.19}$	$0.06^{+0.00}_{-0.00}$
13	$3.58^{+0.01}_{-0.02}$	10.78 ± 1.03	$-0.65^{+0.25}_{-0.27}$	$0.59^{+0.03}_{-0.04}$	81	$3.46^{+0.00}_{-0.00}$	1.80 ± 0.10	$-2.89^{+0.16}_{-0.19}$	$0.07^{+0.00}_{-0.00}$
14	$3.58^{+0.01}_{-0.02}$	12.46 ± 0.23	$0.13^{+0.20}_{-0.26}$	$0.45^{+0.03}_{-0.04}$	82	$3.42^{+0.00}_{-0.00}$	0.00 ± 0.0	$-2.70^{+0.16}_{-0.19}$	$0.04^{+0.00}_{-0.00}$
15	$3.56^{+0.02}_{-0.02}$	1.74 ± 0.06	$-0.41^{+0.26}_{-0.31}$	$0.41^{+0.05}_{-0.04}$	83	$3.45^{+0.00}_{-0.00}$	1.10 ± 0.10	$-3.24^{+0.16}_{-0.19}$	$0.06^{+0.00}_{-0.00}$
16	$3.60^{+0.00}_{-0.01}$	2.26 ± 0.18	$-0.55^{+0.17}_{-0.24}$	$0.70^{+0.01}_{-0.02}$	84	$3.39^{+0.00}_{-0.00}$	1.30 ± 0.10	$-2.89^{+0.16}_{-0.19}$	$0.05^{+0.00}_{-0.00}$
17	$3.56^{+0.02}_{-0.02}$	1.60 ± 0.11	$-0.50^{+0.26}_{-0.31}$	$0.41^{+0.05}_{-0.04}$	85	$3.78^{+0.01}_{-0.01}$	5.94 ± 0.14	$0.70^{+0.17}_{-0.21}$	$1.51^{+0.00}_{-0.00}$
18	$3.53^{+0.02}_{-0.03}$	1.06 ± 0.06	$-0.55^{+0.26}_{-0.34}$	$0.27^{+0.03}_{-0.04}$	86	$3.50^{+0.03}_{-0.04}$	1.93 ± 0.04	$-0.39^{+0.27}_{-0.38}$	$0.18^{+0.04}_{-0.04}$
19	$3.56^{+0.02}_{-0.02}$	0.0 ± 0.0	$-0.74^{+0.18}_{-0.22}$	$0.48^{+0.05}_{-0.05}$	87	$3.58^{+0.01}_{-0.02}$	7.48 ± 0.36	$-0.17^{+0.20}_{-0.26}$	$0.49^{+0.03}_{-0.04}$
20	$3.53^{+0.02}_{-0.03}$	1.69 ± 0.06	$-0.57^{+0.26}_{-0.35}$	$0.27^{+0.03}_{-0.05}$	88	$3.58^{+0.01}_{-0.02}$	2.55 ± 0.04	$-0.35^{+0.23}_{-0.30}$	$0.50^{+0.04}_{-0.05}$
21	$3.56^{+0.02}_{-0.02}$	1.27 ± 0.20	$-0.68^{+0.26}_{-0.31}$	$0.44^{+0.05}_{-0.04}$	89	$3.54^{+0.02}_{-0.02}$	2.53 ± 0.04	$-0.56^{+0.24}_{-0.27}$	$0.35^{+0.04}_{-0.03}$
22	$3.54^{+0.02}_{-0.02}$	1.55 ± 0.11	$-0.66^{+0.28}_{-0.30}$	$0.35^{+0.04}_{-0.03}$	90	$3.50^{+0.03}_{-0.04}$	1.61 ± 0.10	$-0.53^{+0.27}_{-0.38}$	$0.18^{+0.04}_{-0.04}$
23	$3.54^{+0.02}_{-0.02}$	5.37 ± 0.6	$-0.45^{+0.24}_{-0.27}$	$0.36^{+0.04}_{-0.03}$	91	$3.56^{+0.02}_{-0.02}$	1.18 ± 0.02	$-0.14^{+0.26}_{-0.31}$	$0.39^{+0.04}_{-0.03}$
24	$3.50^{+0.03}_{-0.04}$	0.43 ± 0.13	$-0.96^{+0.31}_{-0.28}$	$0.17^{+0.04}_{-0.06}$	92	$3.78^{+0.01}_{-0.01}$	10.90 ± 0.08	$0.84^{+0.18}_{-0.22}$	$1.56^{+0.00}_{-0.00}$
25	$3.56^{+0.02}_{-0.02}$	1.93 ± 0.07	$-0.63^{+0.26}_{-0.31}$	$0.45^{+0.05}_{-0.05}$	93	$3.42^{+0.02}_{-0.01}$	2.87 ± 0.14	$-1.45^{+0.34}_{-0.31}$	$0.04^{+0.01}_{-0.04}$
26	$3.54^{+0.02}_{-0.02}$	1.18 ± 0.08	$-0.87^{+0.28}_{-0.30}$	$0.39^{+0.05}_{-0.04}$	94	$3.56^{+0.02}_{-0.02}$	1.22 ± 0.05	$-0.51^{+0.23}_{-0.28}$	$0.41^{+0.05}_{-0.04}$
27	$3.54^{+0.02}_{-0.02}$	6.90 ± 0.17	$-0.31^{+0.24}_{-0.27}$	$0.33^{+0.03}_{-0.03}$	95	$3.53^{+0.02}_{-0.03}$	1.96 ± 0.07	$-0.47^{+0.23}_{-0.31}$	$0.26^{+0.03}_{-0.05}$
28	$3.54^{+0.02}_{-0.02}$	1.87 ± 0.02	$-0.72^{+0.28}_{-0.30}$	$0.36^{+0.04}_{-0.04}$	96	$3.53^{+0.02}_{-0.03}$	1.76 ± 0.12	$-1.06^{+0.23}_{-0.31}$	$0.30^{+0.04}_{-0.06}$
29	$3.54^{+0.02}_{-0.02}$	1.24 ± 0.02	$-0.78^{+0.28}_{-0.30}$	$0.37^{+0.04}_{-0.04}$	97	$3.53^{+0.02}_{-0.03}$	0.66 ± 0.32	$-0.97^{+0.26}_{-0.29}$	$0.29^{+0.04}_{-0.06}$
30	$3.50^{+0.03}_{-0.04}$	1.10 ± 0.02	$-0.83^{+0.31}_{-0.36}$	$0.18^{+0.04}_{-0.06}$	98	$3.50^{+0.03}_{-0.04}$	0.00 ± 0	$-1.09^{+0.28}_{-0.23}$	$0.17^{+0.05}_{-0.06}$
31	$3.46^{+0.04}_{-0.01}$	2.42 ± 0.15	$-0.81^{+0.40}_{-0.27}$	$0.06^{+0.04}_{-0.02}$	99	$3.53^{+0.02}_{-0.03}$	4.01 ± 0.10	$-0.75^{+0.24}_{-0.33}$	$0.27^{+0.03}_{-0.05}$
32	$3.53^{+0.02}_{-0.03}$	4.69 ± 0.7	$-1.00^{+0.24}_{-0.33}$	$0.30^{+0.04}_{-0.06}$	100	$3.42^{+0.02}_{-0.01}$	7.88 ± 0.31	$-1.31^{+0.34}_{-0.31}$	$0.05^{+0.01}_{-0.00}$
33	$3.46^{+0.04}_{-0.01}$	2.73 ± 0.11	$-0.85^{+0.40}_{-0.27}$	$0.061^{+0.04}_{-0.02}$	101	$3.53^{+0.02}_{-0.03}$	11.29 ± 0.74	$-0.75^{+0.24}_{-0.33}$	$0.28^{+0.04}_{-0.05}$
34	$3.46^{+0.04}_{-0.01}$	2.70 ± 0.08	$-0.92^{+0.40}_{-0.27}$	$0.06^{+0.04}_{-0.02}$	102	$3.53^{+0.02}_{-0.03}$	4.59 ± 0.82	$-1.34^{+0.24}_{-0.33}$	$0.29^{+0.06}_{-0.06}$
35	$3.50^{+0.03}_{-0.04}$	0.41 ± 0.01	$-1.06^{+0.31}_{-0.28}$	$0.18^{+0.05}_{-0.06}$	103	$3.53^{+0.02}_{-0.03}$	15.43 ± 1.27	$-0.42^{+0.23}_{-0.34}$	$0.27^{+0.03}_{-0.05}$
36	$3.53^{+0.02}_{-0.03}$	11.2 ± 1.05	$-0.15^{+0.24}_{-0.33}$	$0.27^{+0.03}_{-0.04}$	104	$3.46^{+0.04}_{-0.01}$	3.28 ± 0.11	$-1.23^{+0.40}_{-0.27}$	$0.06^{+0.06}_{-0.01}$
37	$3.46^{+0.04}_{-0.01}$	3.43 ± 0.10	$-0.85^{+0.40}_{-0.27}$	$0.061^{+0.04}_{-0.02}$	105	$3.46^{+0.04}_{-0.01}$	1.93 ± 0.07	$-1.45^{+0.40}_{-0.27}$	$0.08^{+0.06}_{-0.01}$
38	$3.50^{+0.03}_{-0.04}$	7.78 ± 0.17	$-0.48^{+0.29}_{-0.44}$	$0.18^{+0.04}_{-0.04}$	106	$3.45^{+0.01}_{-0.02}$	2.59 ± 0.05	$-1.41^{+0.24}_{-0.38}$	$0.05^{+0.01}_{-0.01}$
39	$3.50^{+0.03}_{-0.04}$	3.47 ± 0.12	$-0.90^{+0.29}_{-0.44}$	$0.19^{+0.04}_{-0.06}$	107	$3.46^{+0.04}_{-0.01}$	5.61 ± 0.20	$-1.15^{+0.40}_{-0.27}$	$0.08^{+0.05}_{-0.01}$
40	$3.45^{+0.01}_{-0.02}$	2.62 ± 0.10	$-0.93^{+0.24}_{-0.38}$	$0.04^{+0.02}_{-0.01}$	108	$3.46^{+0.04}_{-0.01}$	5.78 ± 0.15	$-1.30^{+0.40}_{-0.27}$	$0.08^{+0.05}_{-0.01}$
41	$3.50^{+0.03}_{-0.04}$	10.26 ± 0.15	$-0.63^{+0.29}_{-0.44}$	$0.18^{+0.04}_{-0.05}$	109	$3.45^{+0.01}_{-0.02}$	3.72 ± 0.15	$-1.53^{+0.24}_{-0.38}$	$0.05^{+0.01}_{-0.01}$
42	$3.50^{+0.03}_{-0.04}$	2.71 ± 0.13	$-0.93^{+0.29}_{-0.44}$	$0.18^{+0.04}_{-0.06}$	110	$3.45^{+0.01}_{-0.02}$	5.57 ± 0.28	$-1.58^{+0.24}_{-0.38}$	$0.05^{+0.01}_{-0.01}$
43	$3.53^{+0.02}_{-0.03}$	12.2 ± 1.42	$-0.68^{+0.24}_{-0.33}$	$0.27^{+0.03}_{-0.04}$	111	$3.50^{+0.03}_{-0.04}$	8.21 ± 0.50	$-1.21^{+0.29}_{-0.44}$	$0.18^{+0.06}_{-0.06}$
44	$3.56^{+0.02}_{-0.02}$	12.52 ± 1.83	$-0.73^{+0.22}_{-0.26}$	$0.48^{+0.05}_{-0.05}$	112	$3.45^{+0.01}_{-0.02}$	0.00 ± 0.00	$-3.18^{+0.16}_{-0.19}$	$0.06^{+0.00}_{-0.01}$
45	$3.45^{+0.01}_{-0.02}$	3.79 ± 0.06	$-0.98^{+0.24}_{-0.38}$	$0.05^{+0.02}_{-0.01}$	113	$3.45^{+0.01}_{-0.02}$	14.30 ± 0.01	$-1.65^{+0.16}_{-0.19}$	$0.05^{+0.01}_{-0.01}$
46	$3.46^{+0.04}_{-0.01}$	0.79 ± 0.07	$-1.20^{+0.40}_{-0.27}$	$0.06^{+0.05}_{-0.01}$	114	$3.39^{+0.00}_{-0.00}$	0.00 ± 0.00	$-2.99^{+0.16}_{-0.19}$	$0.03^{+0.00}_{-0.01}$
47	$3.50^{+0.03}_{-0.04}$	4.19 ± 0.25	$-1.02^{+0.29}_{-0.44}$	$0.18^{+0.05}_{-0.06}$	115	$3.53^{+0.02}_{-0.03}$	6.86 ± 0.21	$-0.62^{+0.24}_{-0.33}$	$0.28^{+0.03}_{-0.04}$
48	$3.58^{+0.01}_{-0.02}$	6.89 ± 0.75	$-1.09^{+0.20}_{-0.26}$	$0.60^{+0.02}_{-0.03}$	116	$3.46^{+0.04}_{-0.01}$	2.43 ± 0.12	$-1.29^{+0.40}_{-0.27}$	$0.08^{+0.06}_{-0.01}$
49	$3.46^{+0.04}_{-0.01}$	1.20 ± 0.10	$-1.19^{+0.40}_{-0.27}$	$0.06^{+0.05}_{-0.01}$	117	$3.42^{+0.02}_{-0.01}$	1.42 ± 0.09	$-1.70^{+0.34}_{-0.31}$	$0.03^{+0.02}_{-0.00}$

Table 5 – *continued*

Source ID	Log T_{eff} (K)	A_v (mag)	Log $L_\star$ (L$_\odot$)	$M_\star$ (M$_\odot$)	Source ID	Log T_{eff} (K)	A_v (mag)	Log $L_\star$ (L$_\odot$)	$M_\star$ (M$_\odot$)
50	$3.46^{+0.04}_{-0.01}$	1.36 ± 0.11	$-1.18^{+0.40}_{-0.27}$	$0.08^{+0.05}_{-0.01}$	118	$3.46^{+0.04}_{-0.01}$	4.48 ± 0.15	$-1.42^{+0.40}_{-0.27}$	$0.07^{+0.06}_{-0.01}$
51	$3.50^{+0.03}_{-0.04}$	4.50 ± 0.11	$-0.90^{+0.29}_{-0.44}$	$0.18^{+0.04}_{-0.06}$	119	$3.46^{+0.04}_{-0.01}$	2.45 ± 0.13	$-1.15^{+0.40}_{-0.27}$	$0.09^{+0.06}_{-0.01}$
52	$3.46^{+0.04}_{-0.01}$	2.69 ± 0.13	$-1.20^{+0.40}_{-0.27}$	$0.08^{+0.05}_{-0.01}$	120	$3.39^{+0.02}_{-0.00}$	0.00 ± 0.00	$-1.94^{+0.16}_{-0.19}$	$0.02^{+0.00}_{-0.00}$
53	$3.45^{+0.01}_{-0.02}$	1.57 ± 0.09	$-1.23^{+0.24}_{-0.37}$	$0.05^{+0.02}_{-0.02}$	121	$3.50^{+0.03}_{-0.04}$	4.03 ± 0.27	$-0.84^{+0.29}_{-0.44}$	$0.19^{+0.04}_{-0.06}$
54	$3.50^{+0.03}_{-0.04}$	5.52 ± 0.10	$-0.97^{+0.29}_{-0.44}$	$0.17^{+0.04}_{-0.06}$	122	$3.50^{+0.03}_{-0.04}$	3.54 ± 0.05	$-1.14^{+0.29}_{-0.44}$	$0.18^{+0.05}_{-0.06}$
55	$3.58^{+0.01}_{-0.02}$	9.65 ± 0.40	$-1.05^{+0.20}_{-0.26}$	$0.61^{+0.02}_{-0.03}$	123	$3.56^{+0.02}_{-0.02}$	0.28 ± 0.14	$-0.50^{+0.26}_{-0.25}$	$0.43^{+0.05}_{-0.04}$
56	$3.42^{+0.02}_{-0.01}$	2.45 ± 0.12	$-1.27^{+0.34}_{-0.30}$	$0.03^{+0.01}_{-0.01}$	124	$3.46^{+0.04}_{-0.01}$	0.00 ± 0.00	$-3.76^{+0.20}_{-0.19}$	$0.04^{+0.04}_{-0.00}$
57	$3.45^{+0.01}_{-0.02}$	2.26 ± 0.08	$-1.35^{+0.24}_{-0.38}$	$0.05^{+0.02}_{-0.02}$	125	$3.46^{+0.04}_{-0.01}$	0.00 ± 0.00	$-1.99^{+0.20}_{-0.19}$	$0.07^{+0.05}_{-0.01}$
58	$3.50^{+0.03}_{-0.04}$	10.56 ± 0.36	$-0.86^{+0.29}_{-0.44}$	$0.18^{+0.04}_{-0.06}$	126	$3.62^{+0.02}_{-0.01}$	3.42 ± 0.25	$-0.19^{+0.18}_{-0.20}$	$0.80^{+0.08}_{-0.05}$
59	$3.46^{+0.04}_{-0.01}$	1.26 ± 0.15	$-1.44^{+0.40}_{-0.27}$	$0.07^{+0.06}_{-0.01}$	127	$3.46^{+0.04}_{-0.01}$	2.70 ± 0.08	$-1.39^{+0.40}_{-0.27}$	$0.08^{+0.06}_{-0.01}$
60	$3.46^{+0.04}_{-0.01}$	2.40 ± 0.09	$-1.34^{+0.40}_{-0.27}$	$0.07^{+0.06}_{-0.01}$	128	$3.50^{+0.03}_{-0.04}$	2.10 ± 0.09	$-1.16^{+0.29}_{-0.44}$	$0.18^{+0.05}_{-0.06}$
61	$3.45^{+0.01}_{-0.02}$	2.90 ± 0.13	$-1.43^{+0.24}_{-0.38}$	$0.05^{+0.01}_{-0.01}$	129	$3.50^{+0.03}_{-0.04}$	6.45 ± 0.54	$-1.63^{+0.29}_{-0.44}$	$0.15^{+0.07}_{-0.05}$
62	$3.45^{+0.01}_{-0.02}$	3.17 ± 0.19	$-1.44^{+0.24}_{-0.38}$	$0.05^{+0.01}_{-0.01}$	130	$3.50^{+0.03}_{-0.04}$	6.72 ± 0.12	$-0.63^{+0.29}_{-0.44}$	$0.18^{+0.05}_{-0.06}$
63	$3.45^{+0.01}_{-0.02}$	1.21 ± 0.10	$-1.57^{+0.24}_{-0.33}$	$0.05^{+0.01}_{-0.01}$	131	$3.41^{+0.01}_{-0.02}$	0.00 ± 0.00	$-2.88^{+0.16}_{-0.19}$	$0.05^{+0.00}_{-0.00}$
64	$3.46^{+0.04}_{-0.01}$	3.46 ± 0.16	$-1.50^{+0.40}_{-0.27}$	$0.06^{+0.06}_{-0.01}$	132	$3.46^{+0.04}_{-0.01}$	0.00 ± 0.00	$-1.45^{+0.20}_{-0.19}$	$0.08^{+0.06}_{-0.01}$
65	$3.46^{+0.04}_{-0.01}$	2.39 ± 0.14	$-1.47^{+0.40}_{-0.27}$	$0.06^{+0.06}_{-0.01}$	133	–	–-	–-	–-
66	$3.46^{+0.04}_{-0.01}$	1.99 ± 0.14	$-1.65^{+0.40}_{-0.27}$	$0.07^{+0.05}_{-0.01}$	134	$3.58^{+0.00}_{-0.00}$	–-	–	–-
67	$3.46^{+0.04}_{-0.01}$	6.26 ± 0.22	$-1.45^{+0.40}_{-0.27}$	$0.06^{+0.06}_{-0.01}$	135	$3.58^{+0.00}_{-0.00}$	–-	–-	–-
68	$3.42^{+0.02}_{-0.01}$	4.27 ± 0.35	$-2.09^{+0.34}_{-0.31}$	$0.02^{+0.01}_{-0.00}$	136	$3.50^{+0.03}_{-0.04}$	4.40 ± 0.00	$-1.22^{+0.29}_{-0.44}$	$0.18^{+0.06}_{-0.05}$
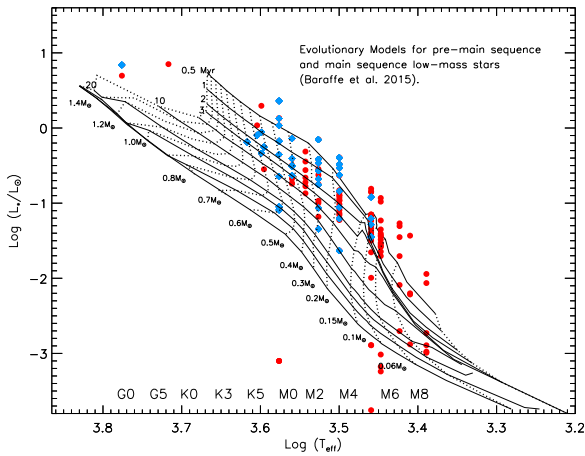
Figure 4. Inferred stellar parameters for IC 348 members (Table 5; Sec. 4.2) with theoretical models from Baraffe et al. (2015) for low-mass young stars overlaid. Solid lines in a descending order are 0.5, 1, 2, 3, 5, 10, 20, 50, and 100 Myr isochrones and dashed lines represent the evolutionary tracks in the range of 0.06 and 1.4 M$_\odot$. The blue diamonds represent IC 348 detected members, while the red circles correspond to non-detections.

fainter than Taurus, and Upper Scorpius is fainter than IC 348, which is not surprising, considering their relative ages and their IR disc fractions (Taurus: 63 per cent, Upper Scorpius: 16 per cent, IC 348: 36 per cent(Ribas et al. 2014)). Also, σ Ori, with an IR disc fraction of 39 per cent, seems to be at an evolutionary stage similar to that of IC 348 in terms of dispersal time-scales.

Distance uncertainty: Recent results for a similar analysis applied to the mm surveys of discs towards other star-forming regions (Taurus, Lupus, Cha I, Ori, Upper Scorpius), also reveal a significant decrease of disc masses with 'age', which has been in-

terpreted as a signature of evolution. However, ages are difficult to determine at early times (<10 Myr) and are highly dependent on the adopted distances and theoretical models (Hillenbrand, Bauermeister & White 2008). Here, we have adopted a 'representative' distance value ($\sim$310 $\pm$ 20 pc) based on those IC 348 objects with high accuracy *Gaia* DR2 parallaxes. However, our IC 348 sample presents a considerable dispersion in distance, even for objects with distance uncertainties < 10 per cent. The closest object IC 348 12 is located at $\sim$214 $\pm$15 pc and the farthest object V$*$ V697 Per is located at $\sim$352 $\pm$ 18 pc. If the distance is less than the adopted value of 310 pc, the target is expected to be even older than 5 Myr. For a distance of $\sim$260 pc, the luminosities would decrease by approximately 30 per cent and the inferred age would be around 3–6 Myr (e.g. Ripepi et al. 2014). Similarly, a larger distance would imply a younger age for a given target. If the distance is actually $\sim$360 pc, the luminosities would increase by approximately 30 per cent and the mean age would be $\sim$1 Myr. Unfortunately, we do not have accurate *Gaia* distance measurements for all IC 348 members studied here, but it is possible that not all targets are actual members of the cluster. Revising the membership status of the targets based on the *Gaia* parallaxes and proper motions is beyond the scope of this paper, but vetting all regions for non-members would certainly be useful for future ALMA studies of discs in clusters. Here, our Monte Carlo simulations are scaled to a distance of 310 pc and we emphasize that the foregoing comparisons of disc luminosity functions are highly dependent on the adopted distance and spectral types.

In addition, adopting spectral types as a proxy for mass also introduces uncertainties as PMS stars, especially higher mass objects, can significantly evolve in spectral type over time. Given that the mm emission from discs depends on the host stellar mass, the results of our statistical analysis can be influenced by the difference in stellar masses at different evolutionary stages and spectral types.
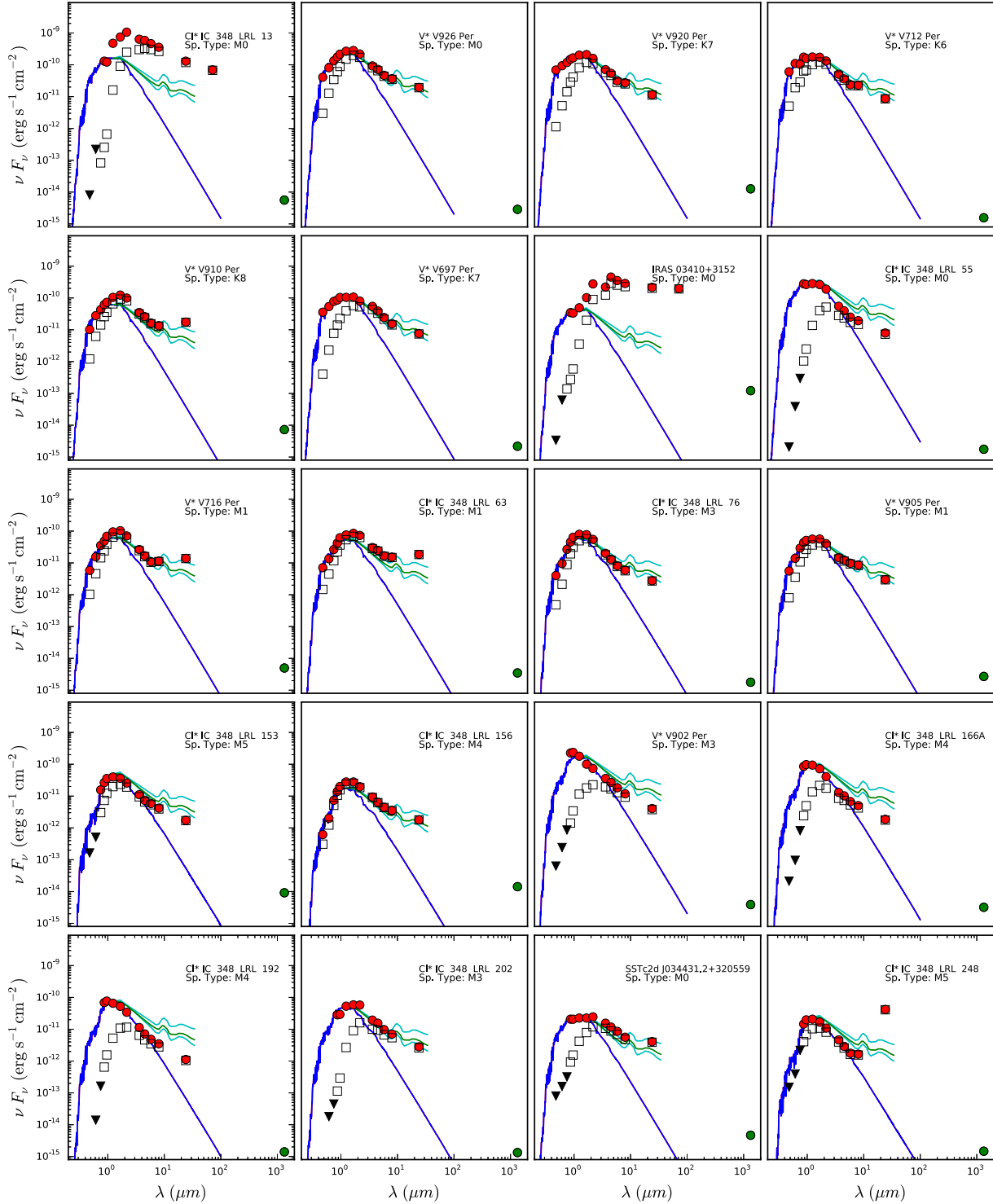
Figure 5. Spectral energy distributions of the sources detected at 1.3 mm in the IC 348 sample. The red dots show photometric data acquired from the literature; the green dots correspond to our ALMA integrated flux density values; the blue lines are the BT-settl spectra model according to the spectral type. A_v values used are in Table 5. The green lines correspond to the median SEDs of K5−M2 CTTSs calculated by Furlan et al. (2006). The black boxes represent the observed optical and IR photometry before correcting for extinction. The black triangles are optical photometry upper limits

5.3 Disc mass versus stellar mass

A commonly used approximation to estimate disc masses is the use of flux densities in the mm-wavelength regime, where the disc luminosity is proportional to the dust mass (Beckwith et al. 1990). In recent years, a Bayesian linear regression approach analysis of

ALMA surveys of star-forming regions at different ages have revealed a positive relationship between dust mass and stellar mass but with a steepening of the $M_{dust} - M_*$ relation. (e.g. Andrews et al. 2013; Ansdell et al. 2016; Pascucci et al. 2016). This method accounts for measurement errors in linear regression for detected and
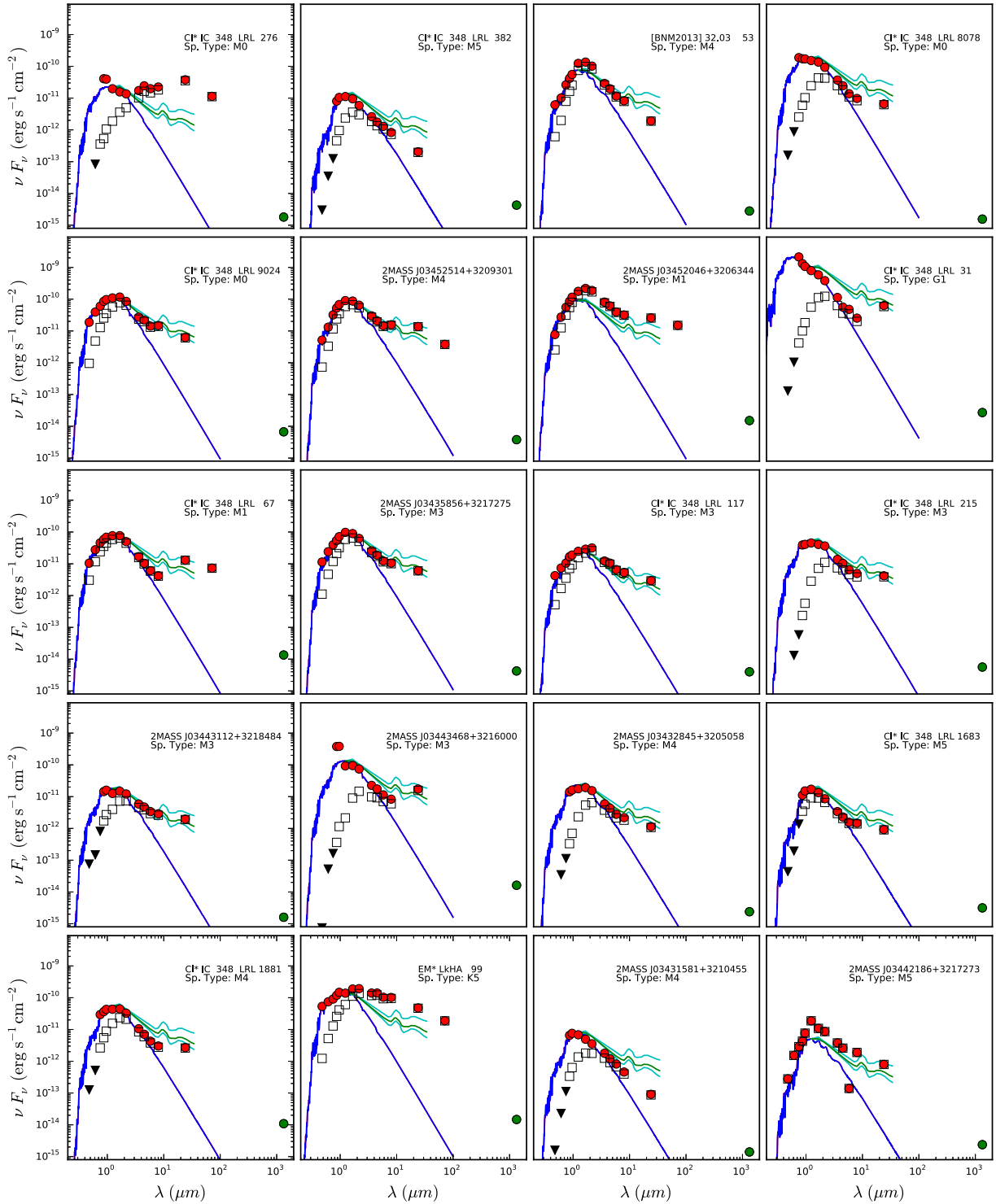
Figure 5 – *continued*

undetected sources, allowing one to correlate measurement errors, and to account for intrinsic scatter in the regression relationship (Kelly 2007). Indeed, studies of Taurus, Lupus, and Chamaeleon I show that the dependence of disc mass on stellar mass is similar at an age of ∼1–3 Myr, while older regions such as σ Ori and Upper Scorpius present a steeper disc mass vs. stellar mass relation (Pascucci et al. 2016; Ansdell et al. 2017). The steepening of this relation with age has been interpreted in terms of an efficient inward drift

of mm-sized grains (Pascucci et al. 2016). However, the parameters describing the dependence of disc mass on stellar mass are very sensitive to the mm-detection fraction and the treatment of the upper limits. In the case of IC 348, the detection fraction is low (∼30 per cent) and is a strong function of stellar mass. As a result, most of the detections are restricted to a narrow range of stellar masses. Given these issues, a linear regression fit is not accurate enough to allow a meaningful comparison to other star-forming regions. Nev-
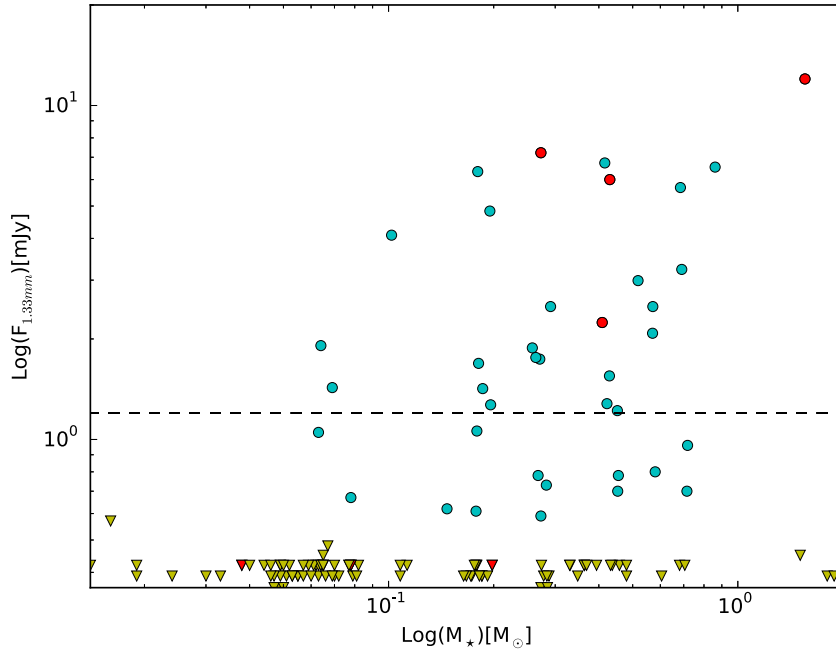
Figure 6. 1.3 mm continuum flux as a function of stellar mass for IC 348 Class II sources. The cyan circles and yellow triangles represent detected sources and upper limits for non-detected sources, respectively. Four transitional discs (red circles) are among the most massive discs in the sample, while there are four transitional discs (red triangles) among the non-detected sources. The horizontal dashed-line indicates the flux level corresponding to a disc mass of ~ 1 $M_{\rm Jup}$ assuming a gas to dust mass ratio of 100.
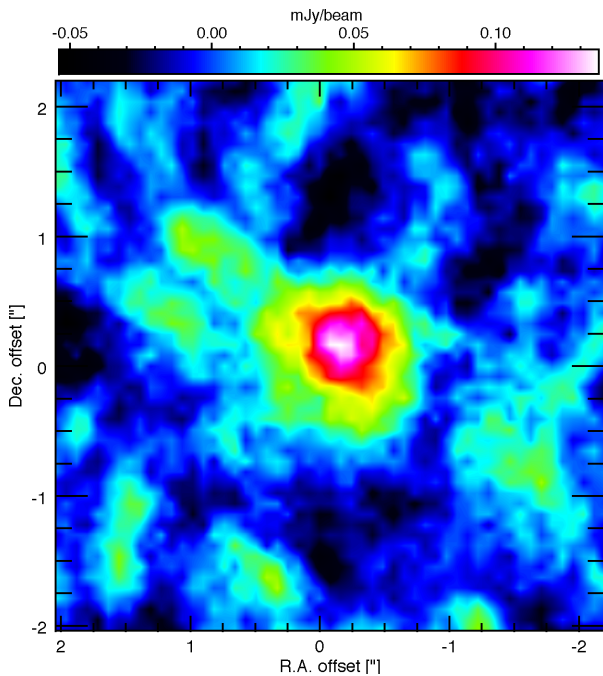
Figure 7. Stacked image for the 96 non-detections, clearly showing a detection at the 6σ level.

Figure 8. Distribution of stellar spectral types for the detected and non-detected sources in IC 348 targeted by our ALMA survey (Tables 2 and 3).

ertheless, we report the resulting parameters from the 'standard' methodology used in the previous studies mentioned above.

Considering all IC 348 sources in our ALMA sample, we derive slope and intercept values of $\beta = 0.90 \pm 0.21$ and $\alpha = 0.37 \pm 0.18$, where β and α are the slope and intercept, respectively. Fig. 10 shows the linear fit obtained from the Bayesian method. Because

of the difficulty in obtaining a reliable fit, we only use σ Ori as a comparison to illustrate differences between our fitting and other investigations with a wider mass range. The linear regression for σ Ori data generated values of 1.95 ± 0.37 and 1.00 ± 0.20 for β and α, respectively, and an intrinsic scatter value (δ) of 0.65 ± 0.15, consistent with the values estimated by Ansdell et al. (2017). The fitted linear regression for IC 348 provides a large intrinsic scatter of $\delta = 0.81 \pm 0.15$. Similar large intrinsic dispersions were estimated for Taurus, Lupus, Cha I, σ Ori, and Upper Scorpius (Pascucci et al. 2016; Ansdell et al. 2017). As previously suggested by Pascucci et al. (2016), the dispersion can be an intrinsic property of the disc population (i.e. disc masses, dust temperatures, and grain sizes) reflected in the diversity of planetary systems.
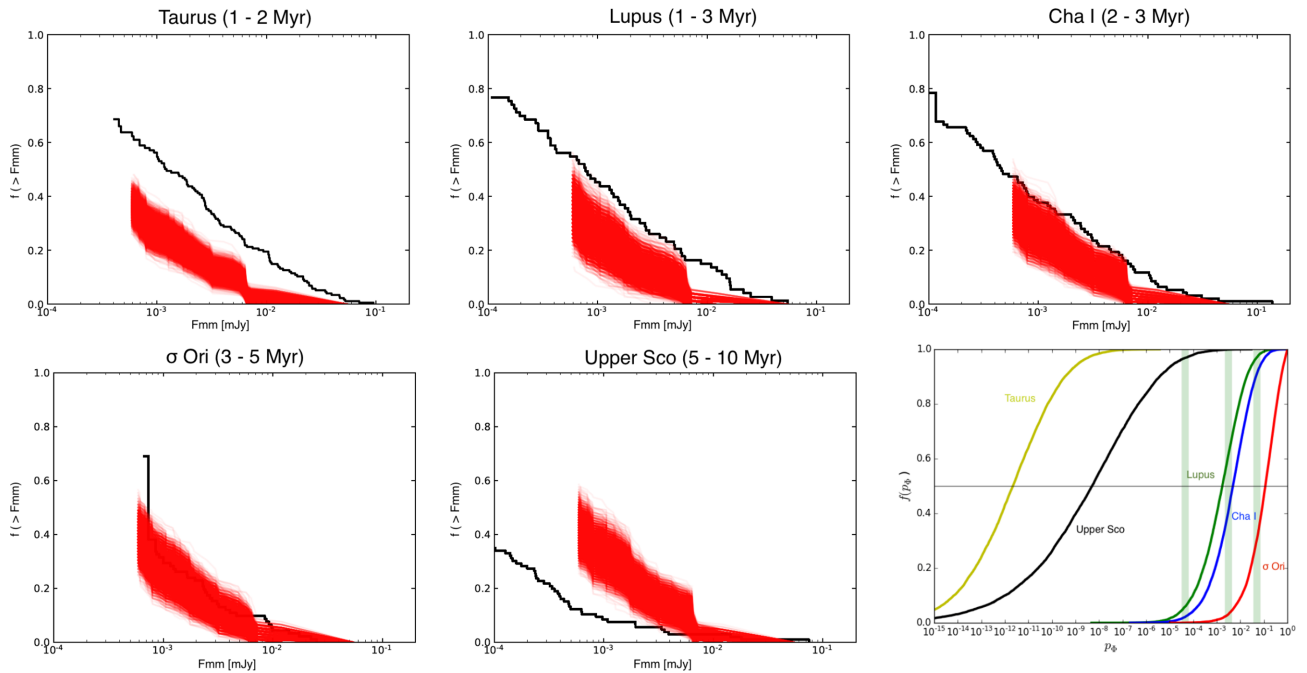
Figure 9. Cumulative Distribution Functions of the disc luminosities in IC 348 (red) and the 10^6 synthetic 'reference' disc draws, Taurus (1–2 Myr), Lupus (1–3 Myr), Cha I (2–3 Myr), σ Ori (3–5 Myr), and Upper Scorpius (5–10 Myr), in black colour. At the right bottom, the comparison between the disc luminosity distribution of IC 348 and the 'reference' sample shows the probability that IC 348 and the 'reference' sample belong to the same population. The vertical green bars indicate the nominal 2, 3, and 4σ probabilities.
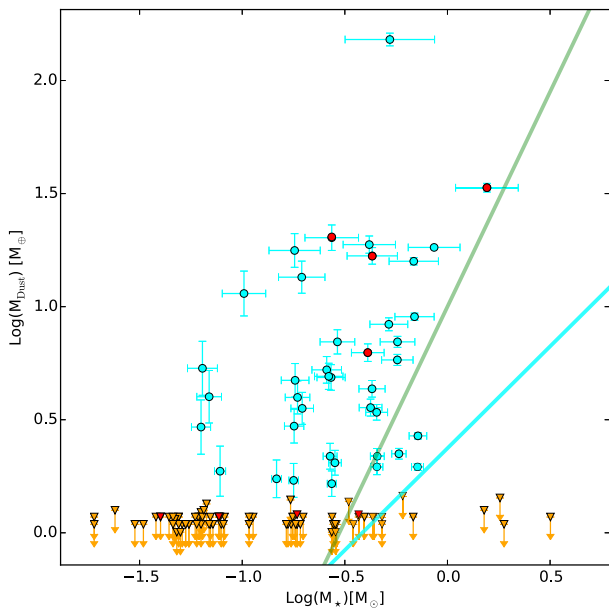
Figure 10. Disc dust mass as a function of stellar mass for IC 348 region. The cyan circles represent the detected sources, while the yellow triangles are 4σ upper limits for non-detections. TDs are displayed by the red circles and triangles, same as Fig. 6. The cyan and green solid lines represent the Bayesian linear regression obtained for IC 348 and σ Ori, respectively; see Section 5.3.

Moreover, $M_{\rm dust}$ measurements are subject to systematic uncertainties in the assumed parameters, such as distances to the star-forming regions. One can hence expect these results for $M_{\rm dust}$ to change with the availability of *Gaia* DR2 data. In addition, obtaining a realistic dust temperature profile is important in the accuracy

of estimates of $M_{\rm dust}$, and to this purpose, a high-resolution data are required to generate those profiles. However, as shown by Tazzari et al. (2017), assuming a constant $T_{\rm dust}$ of $\sim$20 K, provides estimates of $M_{\rm dust}$ that are in good agreement with the results of more detailed modeling over a wide range of stellar masses, 0.1–2.0M$_\odot$.

5.4 CO emission from IRAS 03410+3152

The brightest mm source in our sample, IRAS 03410+3152, which has a bolometric temperature of 463 K and luminosity of 1.6 L$_\odot$ (Hatchell et al. 2007), was observed previously with the Submm Array by Lee et al. (2011). They detected a bipolar shape in the ^{12}CO emission, with prominent emission outflow lobes and a moderate opening angle. From our observations at a resolution of 0.3 arcsec, we are able to estimate PA, mass, and kinematics of the outflow following the process presented in Ruíz-Rodríguez et al. (2017). Here, we used the ^{13}CO emission to correct for the CO optical depth and estimated the mass, momentum and kinetic energy of the outflow, see Fig. 12. Using the C^{18}O line, we estimated a systemic velocity of $\sim$8.0 km s^{-1}. Because ^{12}CO traces the bipolar and extension cavities of the outflow, we drew a line along the rotation axis to estimate a PA of $\sim$−155° north through east. Additionally, taking the extent of $\sim$3800 au (14 arcsec) and maximum speed of the ^{12}CO emission, we estimated a kinematic age of 1800 yr.

To compute the ^{12}CO mass, we apply the correction factor to all the channels with ^{13}CO detection above 4σ. In order to ensure emission only from the outflow, we built a mask around IRAS 03410+3152 of radius 3.0 arcsec, where emission inside this area was removed from the integration. Thus, separating the red- and blue-shifted components, the blue-shifted outflow kinematics were estimated by integrating channels in the range between 5.0 and 8.0 km s^{-1} for ^{12}CO and, 5.0 and 8.0 km s^{-1} for ^{13}CO. The range of channels in the redshifted emission is between 9.5 and 17.5 km s^{-1}
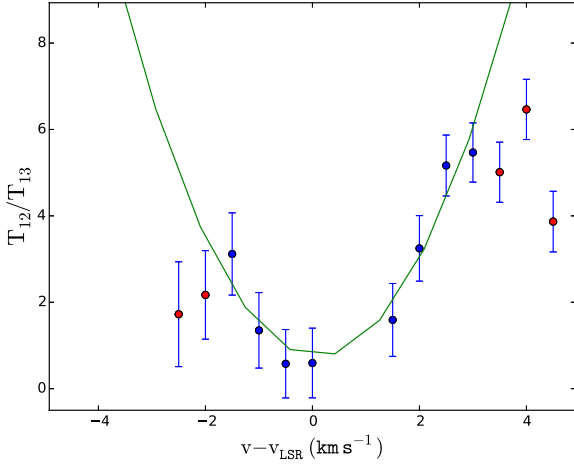
Figure 11. Intensity ratio between ^{12}CO and ^{13}CO function of velocity. The green solid curve is the best-fit second-order polynomial using the blue data points, more details in Ruíz-Rodríguez et al. (2017)
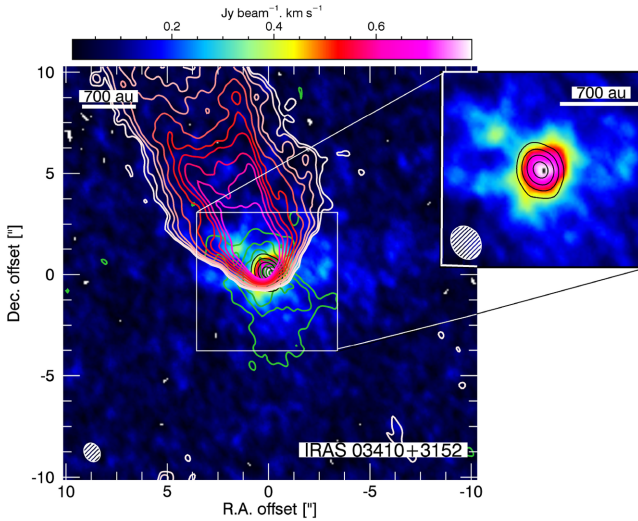

Figure 12. ^{13}CO intensity map (moment-0) of IRAS 03410+3152 integrated over the velocity range of 5.0–11.5 km s^{-1}. The black contours show the 1.3 mm continuum emission around IRAS 03410+3152 at 10, 40, 60, and 80 × rms (0.15 mJy beam^{-1}). The green and red contours show the blue- and red- shifted moment-0 of the ^{12}CO line, respectively, at 20, 40, 80, 160 × 3σ levels. These blue- and red- shifted intensity maps are integrated over the velocity range of 5.0–8 km s^{-1} and 9.5–17.5 km s^{-1}, respectively. The synthesized beam of 0.77 arcsec × 0.63 arcsec with PA = 20.33 deg. is shown in the lower left corner. The upper right inset is a closeup (±2.5 arcsec) of the central object.

for ^{12}CO and, 9.5 and 11.5 km s^{-1} for ^{13}CO. To apply the correction factor to all the channels with ^{12}CO detection, we extrapolate values from a parabola fitted to the weighted mean values, where the minimum ratio value was fixed at zero velocity. In the fitting process, we did not include those data points presented as red dots in Fig. 11, because at these velocities ^{12}CO starts becoming optically thin. The fitted parabola has the form:

$$\frac{T_{12}}{T_{13}} x00A0; = x00A0; 0.11 + 0.40(v - v_{LSR})^2. \tag{2}$$

Table 6 shows the estimates at temperatures of 20 and 50 K and without correcting for inclination effects. Correcting for the

^{12}CO optical depth increases the estimated mass of the outflow, the momentum, and the kinetic energy by factors of 7.5–43, 5–27, and 4–23, respectively, at a temperature of 20 K.

IRAS 03410+3152 has been identified as an optically thick Class II protostar with a slope of $\alpha_{3.6-8.0\,\mu m} \sim -0.006$ (Lada et al. 2006). While the highly dereddened SED peaking in the mid-infrared clearly shows that IRAS 03410+3152 is still embedded, the presence of energetic outflows suggests that this object could be a Class I. Furthermore, the estimated outflow mass on the order of 10^{-2} M$_\odot$ is consistent with the highest mass estimates of previously reported Class 0 and I outflows, after correcting for optical depth effects (Dunham et al. 2014). The differences between these estimates can be attributed to the higher ALMA sensitivities, which facilitate the detection of weak and high-velocity emission from the outflows, thus integrating over high-resolution spectra. In Table 6, note that the measured mass of the blue-shifted outflow is a factor of ~2 lower than that of the red-shifted outflow, indicating possible differences in the environment between the cavities.

6 SUMMARY

We have observed 136 Class II members of the young stellar cluster IC 348 with ALMA at 1.3 mm. We reach a dust mass sensitivity of 1.3 M$_\oplus$ (3σ) and detect a total of 40 discs. The detection rate is a strong function of spectral type, as expected from the known dependence of disc mass on stellar mass. A stacking analysis of the 96 objects that were not individually detected yielded a clear 6σ detection of 0.14 mJy, indicating that these discs have a typical dust mass of just ≲0.4 M$_\oplus$, even though their infrared SEDs remain optically thick and show little signs of evolution.

We compare the disc luminosity function in IC 348 to those in younger and older regions and see a clear evolution in the dust masses between 1 and 5–10 Myr. Based on the statistics of extrasolar planets (Gaidos et al. 2016; Howard et al. 2012; Burke et al. 2015), a stellar cluster like IC 348 with ~400 members dominated by low-mass stars should form a very small fraction of systems (≲5 per cent) with giant planets, which is consistent with the number of discs with masses > 1 M_{Jup} in the cluster and the presence of transition discs among this small population. The rest of the members should mostly form small rocky planets, consuming most of the primordial dust by the age of the cluster. For the brightest mm source in our sample, IRAS 03410+3152, we are able to estimate PA, mass, and kinematics of the outflow. These estimates are characteristic of a Class-I type object.

Table 6. Mass, momentum, luminosity, and kinetic energy of the outflow and envelope.

Isotope	Property	Red shifted[1]		Blue shifted[2]	
		50 (K)	20 (K)	50 (K)	20 (K)
^{12}CO	Mass (10^{-2} $M_\odot$)	23.50 (163.40)	15.89 (110.40)	1.68 (77.73)	1.13 (52.53)
	Mass loss (10^{-6} $M_\odot$ yr^{-1})	131.18 (911.69)	88.60 (616.14)	9.36 (433.80)	6.33 (293.00)
	Momentum (10^{-2} $M_\odot$ km s^{-1})	106.00 (556.6)	72.09 (376.21)	1.53 (40.95)	1.04 (27.67)
	Energy (10^{42} ergs.)	55.38 (220.39)	37.43 (149.00)	0.25 (5.50)	0.16 (3.69)
	Luminosity ($10^{-2} L_\odot$)	25.46 (101.33)	17.21 (68.48)	0.11 (2.52)	0.08 (1.70)
^{13}CO	Mass (10^{-2} $M_\odot$)	0.16	0.11	0.08	0.55
	Mass loss (10^{-6} $M_\odot$ yr^{-1})	0.90	0.60	4.63	3.10
	Momentum (10^{-2} $M_\odot$ km s^{-1})	0.27	0.18	0.17	0.11
	Energy (10^{41} ergs.)	0.49	0.33	0.24	0.16
	Luminosity (10^{-2} $L_\odot$)	0.02	0.02	0.01	0.01

[1] Blue-shifted outflow kinematics were estimated after a cut above 4σ and integration of channels between 5.0 and 8.0 km s^{-1} for ^{12}CO and 5.0 and 8.0 km s^{-1} for ^{13}CO.

[2] Red-shifted outflow kinematics were estimated with a threshold value above 4σ and integration of channels between 9.5 and 17.5 km s^{-1} for ^{12}CO, and 9.5 and 11.5 km s^{-1} for ^{13}CO.

[3] Parameters inside the parentheses correspond to the computed values after applying the correction factors for optical depth effects to all the channels with ^{13}CO detection above 4σ.

REFERENCES

Alcalá J. M. et al., 2014, A&A, 561, A2

Alexander R., Pascucci I., Andrews S., Armitage P., Cieza L., 2014, in Beuther H., Klessen R.S., Dullemond C.P., Henning T., eds, Protostars and Planets VI, Univ. Arizona Press, Tucson, AZ, p. 475

Alibert Y., Mordasini C., Benz W., 2011, A&A, 526, A63

Allard F., 2014, in Booth M., Matthews B. C., Graham J. R., eds, Proc. IAU Symp. 299, Exploring the Formation and Evolution of Planetary Systems, p. 271

Andrews S. M., Williams J. P., 2005, ApJ, 631, 1134

Andrews S. M., Rosenfeld K. A., Kraus A. L., Wilner D. J., 2013, ApJ, 771, 129

Ansdell M. et al., 2016, ApJ, 828, 46

Ansdell M., Williams J. P., Manara C. F., Miotello A., Facchini S., van der Marel N., Testi L., van Dishoeck E. F., 2017, AJ, 153, 240

Baraffe I., Homeier D., Allard F., Chabrier G., 2015, AAP, 577, A42

Barenfeld S. A., Carpenter J. M., Ricci L., Isella A., 2016, ApJ, 827, 142

Beckwith S. V. W., Sargent A. I., Chini R. S., Guesten R., 1990, AJ, 99, 924

Bonfils X. et al., 2013, A&A, 549, A109

Bressan A., Marigo P., Girardi L., Salasnich B., Dal Cero C., Rubele S., Nanni A., 2012, MNRAS, 427, 127

Burke C. J. et al., 2015, ApJ, 809, 8

Cardelli J. A., Clayton G. C., Mathis J. S., 1989, ApJ, 345, 245

Cieza L. et al., 2007, ApJ, 667, 308

Cieza L. A., Schreiber M. R., Romero G. A., Williams J. P., Rebassa-Mansergas A., Merín B., 2012, ApJ, 750, 157

Cieza L., Williams J., Kourkchi E., Andrews S., Casassus S., Graves S., Schreiber M. R., 2015, MNRAS, 454, 1909

Comeron F., 2008, in Reipurth B., ed., The Lupus Clouds, Handbook of Star Forming Regions II. The Southern Sky ASP Monograph Publications, p. 295

Currie T., Kenyon S. J., 2009, AJ, 138, 703

Dunham M. M., Arce H. G., Mardones D., Lee J.-E., Matthews B. C., Stutz A. M., Williams J. P., 2014, ApJ, 783, 29

Espaillat C. et al., 2012, ApJ, 747, 103

Evans N. J., II, Allen L. E., Blake G. A., Boogert A. C. A., Bourke T., Harvey P. M., Young C. H., Young K. E., 2003, PASP, 115, 965

Feigelson E. D., Nelson P. I., 1985, ApJ, 293, 192

Furlan E. et al., 2006, ApJS, 165, 568

Gaidos E., Mann A. W., Kraus A. L., Ireland M., 2016, MNRAS, 457, 2877

Greene T. P., Wilking B. A., Andre P., Young E. T., Lada C. J., 1994, ApJ, 434, 614

Gustafsson B., Edvardsson B., Eriksson K., Jørgensen U. G., Nordlund Å., Plez B., 2008, A&A, 486, 951

Hatchell J., Fuller G. A., Richer J. S., Harries T. J., Ladd E. F., 2007, A&A, 468, 1009

Herbig G. H., 1954, PASP, 66, 19

Herbig G. H., 1998, ApJ, 497, 736

Hildebrand R. H., 1983, QJRAS, 24, 267

Hillenbrand L. A., Bauermeister A., White R. J., 2008, in van Belle G., ed., ASP Conf. Ser., Vol. 384, 14th Cambridge Workshop on Cool Stars, Stellar Systems, and the Sun. Astron. Soc. Pac., San Francisco, p. 200

Howard A. W. et al., 2012, ApJs, 201, 15

Johnson J. A., Aller K. M., Howard A. W., Crepp J. R., 2010, PASP, 122, 905

Kelly B. C., 2007, ApJ, 665, 1489

Kenyon S. J., Hartmann L., 1995, APJs, 101, 117

Lada C. J. et al., 2006, AJ, 131, 1574

Lada E. A., Lada C. J., 1995, AJ, 109, 1682

Lee N., Williams J. P., Cieza L. A., 2011, ApJ, 736, 135

Luhman K. L., 1999, ApJ, 525, 466

Luhman K. L., 2003, in Martín E., ed., Proc. IAU Symposium, Vol. 211, Brown Dwarfs. ASP, San Francisco, p. 103

Luhman K. L., 2007, ApJS, 173, 104

Luhman K. L., Rieke G. H., Lada C. J., Lada E. A., 1998, ApJ, 508, 347

Luhman K. L., Stauffer J. R., Muench A. A., Rieke G. H., Lada E. A., Bouvier J., Lada C. J., 2003, ApJ, 593, 1093

Luhman K. L., McLeod K. K., Goldenson N., 2005, ApJ, 623, 1141
Luhman K. L., Esplin T. L., Loutrel N. P., 2016, ApJ, 827, 52
Luri X. et al., 2018, A&A, in press
Magnier E. A. et al., 2013, ApJs, 205, 20
Mathis J. S., Cardelli J. A., 1990, BAAS, 22, 861
McMullin J. P., Waters B., Schiebel D., Young W., Golap K., 2007, in Shaw R. A., Hill F., Bell D. J., eds, Astronomical Society of the Pacific Conference Series, Vol. 376, Astronomical Data Analysis Software and Systems XVI, p. 127
Mordasini C., Alibert Y., Benz W., Klahr H., Henning T., 2012, AAP, 541, A97
Muench A. A., Lada C. J., Luhman K. L., Muzerolle J., Young E., 2007, AJ, 134, 411
Nagel E., D'Alessio P., Calvet N., Espaillat C., Sargent B., Hernández J., Forrest W. J., 2010, ApJ, 708, 38
Oliveira J. M., Jeffries R. D., Kenyon M. J., Thompson S. A., Naylor T., 2002, A&A, 382, L22
Owen J. E., Clarke C. J., 2012, MNRAS, 426, L96
Pascucci I., Testi L., Herczeg G. J., Long F., Manara C. F., Hendler N., Mulders G. D., Krijt S., 2016, ApJ, 831, 125

Pecaut M. J., Mamajek E. E., 2013, ApJs, 208, 9
Pecaut M. J., Mamajek E. E., Bubar E. J., 2012, ApJ, 746, 154
Ribas Á., Merín B., Bouy H., Maud L. T., 2014, A&A, 561, A54
Ripepi V. et al., 2014, MNRAS, 437, 906
Ruíz-Rodríguez D. et al., 2017, MNRAS, 466, 3519
Ruíz-Rodríguez D., Ireland M., Cieza L., Kraus A., 2016, MNRAS, 463, 3829
Sicilia-Aguilar A., Bohac C., Bouwman J., Hartmann L., Henning T., Watson D., 2006, Dust and Gas in Planet-Forming discs: Tracing the Grains in Transitional and Evolved Systems. Spitzer Proposal
Skrutskie M. F. et al., 2006, AJ, 131, 1163
Tazzari M. et al., 2017, A&A, 606, A88
van der Marel N. et al., 2018, ApJ, 854, 1
Williams J. P., Cieza L. A., 2011, ARA&A, 49, 67

This paper has been typeset from a TEX/LATEX file prepared by the author.